

The Pennsylvania State University
APPLIED RESEARCH LAB
PO Box 30
State College, PA 16804

**Sensorless Electric Drive for Integral Horsepower
Permanent Magnet Synchronous Motor**

by

Todd D. Batzel
Research Associate

Technical Report No. TR 01-005
October 2001

Support by:
Office of Naval Research
Code ONR 334

L.R. Hettche, Director
Applied Research Laboratory

Approved for public release; distribution unlimited.

20011113 098

REPORT DOCUMENTATION PAGE

Form Approved
OMB No. 0704-0188

Public reporting burden for this collection of information is estimated to average 1 hour per response, including the time for reviewing instructions, searching data sources, gathering and maintaining the data needed, and completing and reviewing the collection of information. Send comments regarding this burden estimate or any other aspect of this collection of information, including suggestions for reducing this burden to Washington Headquarters Service, Directorate for Information Operations and Reports, 1215 Jefferson Davis Highway, Suite 1204, Arlington, VA 22202-4302, and to the Office of Management and Budget, Paperwork Reduction Project (0704-0188) Washington, DC 20503.

PLEASE DO NOT RETURN YOUR FORM TO THE ABOVE ADDRESS.

1. REPORT DATE (DD-MM-YYYY) 15 October 2001		2. REPORT DATE		3. DATES COVERED (From - To) June 2000 - October 2001	
4. TITLE AND SUBTITLE Sensorless Electric Drive for Integral Horsepower Permanent Magnet Synchronous Motor				5a. CONTRACT NUMBER	
				5b. GRANT NUMBER N00014-00-G-0058/007	
				5c. PROGRAM ELEMENT NUMBER	
6. AUTHOR(S) Batzel, Todd D.				5d. PROJECT NUMBER 9663	
				5e. TASK NUMBER	
				5f. WORK UNIT NUMBER	
7. PERFORMING ORGANIZATION NAME(S) AND ADDRESS(ES) Applied Research Laboratory P.O. Box 30 State College, PA 16804				8. PERFORMING ORGANIZATION REPORT NUMBER TR 01-005	
9. SPONSORING/MONITORING AGENCY NAME(S) AND ADDRESS(ES) Naval Undersea Warfare Center				10. SPONSOR/MONITOR'S ACRONYM(S) NUWC	
				11. SPONSORING/MONITORING AGENCY REPORT NUMBER	
12. DISTRIBUTION AVAILABILITY STATEMENT Approved for Public Release					
13. SUPPLEMENTARY NOTES					
14. ABSTRACT The permanent magnet synchronous motor (PMSM) is increasingly playing an important role in electric propulsion systems due to its many advantages over competing technologies. For successful implementation of the PMSM, rotor position and speed information are required. A resolver or encoder attached to the shaft of the machine usually provides this information. Many applications, however, cannot tolerate the use of the position sensor due to space and weight limitations, reliability concerns, or packaging issues. Thus, there has been an intense interest in the development of a so-called <i>position sensorless</i> drive, where the PMSM stator itself is used as the rotor position sensor. In this work, a previously developed sensorless electric drive technique ['] is applied to a high power permanent magnet machine. The sensorless drive hardware implementation is presented in detail. A set of experiments is used to quantify the performance of the sensorless drive approach under a wide variety of operating conditions, and implementation issues and results are discussed. The developed sensorless electric drive serves as a technology demonstrator for future naval applications.					
15. SUBJECT TERMS Sensorless, Electric Drive, Permanent Magnet Synchronous Motor					
16. SECURITY CLASSIFICATION OF:			17. LIMITATION OF ABSTRACT	18. NUMBER OF PAGES	19a. NAME OF RESPONSIBLE PERSON
a. REPORT	b. ABSTRACT	c. THIS PAGE			Todd D. Batzel
U	U	U			19b. TELEPHONE NUMBER (include area code) 814-863-7338

Abstract

The permanent magnet synchronous motor (PMSM) is increasingly playing an important role in electric propulsion systems due to its many advantages over competing technologies. For successful implementation of the PMSM, rotor position and speed information are required. A resolver or encoder attached to the shaft of the machine usually provides this information. Many applications, however, cannot tolerate the use of the position sensor due to space and weight limitations, reliability concerns, or packaging issues. Thus, there has been an intense interest in the development of a so-called *position sensorless* drive, where the PMSM stator itself is used as the rotor position sensor. In this work, a previously developed sensorless electric drive technique [1] is applied to a high power permanent magnet machine. The sensorless drive hardware implementation is presented in detail. A set of experiments is used to quantify the performance of the sensorless drive approach under a wide variety of operating conditions, and implementation issues and results are discussed. The developed sensorless electric drive serves as a technology demonstrator for future naval applications.

Table of Contents

1	INTRODUCTION	1
1.1	Statement of Problem	1
1.2	Statement of Purpose	1
1.3	Organization of Report	2
2	ROTOR POSITION ESTIMATION	2
2.1	Sensorless PMSM Model	2
2.2	Rotor Position Observer	4
2.3	Angular Velocity Estimation	5
2.3.1	Quasi Steady State Velocity Estimation	5
2.3.2	Time Derivative of Estimated Rotor Angle	5
2.3.3	Adaptive Velocity Estimation	6
2.4	Rotor Position Observer Pole Placement	7
2.5	Estimation Error Analysis	9
2.5.1	Effect of Angular Velocity Estimation on Rotor Angle Estimation Accuracy	10
2.5.2	Effect of Stator Resistance Uncertainty on Angle Estimation Accuracy	13
2.5.3	Effect of Stator Inductance Uncertainty on Angle Estimation Accuracy	16
2.5.4	Effect of PM Flux Linkage Uncertainty on Angle Estimation Accuracy	19
2.5.5	Effect of Stator Voltage and Current Measurement Errors	20
2.5.5.1	Voltage Measurement Error	20
2.5.5.2	Current Measurement Errors	23
2.6	Eigenvalue Selection Strategy	24
3	SENSORLESS DRIVE IMPLEMENTATION	25
3.1	Control Implementation	25
3.1.1	Current Controller	27
3.1.2	Velocity Controller	31
3.2	Hardware and Algorithm Implementation	33
3.2.1	Computing Hardware	33
3.3	Software Development	33
3.3.1	Sensors	35
3.3.1.1	Voltage Measurements	35
3.3.1.2	Current Measurements	36
3.3.2	Power Output Stage	37
3.3.3	Output Filter	38
3.4	PMSM Motor	39
4	SENSORLESS PMSM EXPERIMENTAL RESULTS	41
4.1	Experimental System	41
4.2	Experimental Results	42
4.2.1	Steady State Rotor Position Estimation Accuracy	42
4.2.1.1	Low Speed Operation	44
4.2.1.2	Steady State Rotor Position Estimation Robustness	46
4.2.2	Transient Rotor Position Estimation Accuracy	53

4.2.2.1	Startup of Sensorless PMSM	53
4.2.2.2	Speed Reversal	54
4.3	Acoustic Performance	57
5	CONCLUSIONS	57
6	ACKNOWLEDGEMENTS	58
7	REFERENCES	59

List of Figures

Figure 1.	Velocity estimation correction block.	6
Figure 2.	Block diagram of rotor position estimator.....	7
Figure 3.	Effect of state estimation error on angle estimation.....	9
Figure 4.	Angle estimation error due to $\pm 10\%$ velocity error, slow observer poles.....	13
Figure 5.	Angle estimation with 10 percent velocity error, fast observer poles.....	13
Figure 6.	Resistance uncertainty effect on angle estimation: $\Delta R = 1\Omega$, heavily loaded..	16
Figure 7.	Stator inductance uncertainty effect on rotor angle estimation.	19
Figure 8.	Effect of unbalanced voltage sensor scaling error.	22
Figure 9.	Effect of voltage measurement offset of angle estimation.	22
Figure 10.	Block diagram of sensorless PMSM drive system.....	26
Figure 11.	Actual sensorless PMSM drive.	26
Figure 12.	PMSM current control block diagram.....	29
Figure 13.	Current controller performance during steady state.....	30
Figure 14.	Current controller performance during speed reversal transient.....	30
Figure 15.	Current control during startup transient.....	31
Figure 16.	Sensorless velocity control – steady state 300 rpm.....	32
Figure 17.	Sensorless velocity control – speed reversal.....	32
Figure 18.	Block diagram of prototype sensorless drive hardware.	34
Figure 19.	Dual-DSP processing hardware- top view (left), bottom view (right).....	34
Figure 20.	Program flow diagram for sensorless drive implementation.	35
Figure 21.	Block diagram of direct phase voltage measurement.....	36
Figure 22.	Current sensors and main breaker.	37
Figure 23.	Inverter (left) and AC/DC converter (right) used in sensorless electric drive.	38
Figure 24.	Block diagram of LC filter.....	39
Figure 25.	Line voltage without LC filter (left) and with LC filter (right).	39
Figure 26.	Diagram of PMSM winding configuration.	40
Figure 27.	70 HP PMSM used in sensorless electric drive studies.....	40
Figure 28.	Motor (foreground) and load (background) used in sensorless drive studies.	42
Figure 29.	Angle estimation accuracy versus speed for low speed winding configuration.	43
Figure 30.	Angle estimation accuracy versus speed for high speed winding configuration.	43
Figure 31.	Estimation accuracy at 30 RPM, 10 ft-lb – low speed winding configuration.	45

Figure 32. Estimation accuracy at 50 RPM, 15 ft-lb – low speed winding configuration.	45
Figure 33. Estimation accuracy versus load torque at constant speed – low speed winding configuration.	47
Figure 34. Estimation accuracy versus load torque at constant speed – high speed winding configuration.	47
Figure 35. Estimation accuracy versus load at Constant Speed - low speed windings with stator inductance detuned by 50%.	48
Figure 36. Estimation accuracy with actual (top), and detuned resistance values.	49
Figure 37. Angle estimation performance at 200 RPM, 100 ft-lb – with line filter.	50
Figure 38. Angle estimation performance at 200 RPM, 100 ft-lb – without line filter.	50
Figure 39. Measurements and state estimation for 500 rpm, 400 ft-lb load.	51
Figure 40. Measurements and state estimation for 900 rpm, 400 ft-lb load.	52
Figure 41. Startup from zero speed with load of 80 ft-lb at 200 RPM.	54
Figure 42. Startup from zero speed with load of 180 ft-lb at 300 RPM.	55
Figure 43. Speed reversal of PMSM – state variables and measured quantities.	56

List of Tables

Table I. Electrodynamics Corp. motor parameters (low-speed winding configuration)..	41
Table II Electrodynamics Corp. motor parameters (high-speed winding configuration).	41

List of Symbols

<u>Abbreviation</u>	<u>Variable</u>	<u>Unit</u>
λ	flux linkage	Wb=V-s
ω	angular frequency	rad/s
θ	angle	rad
$s = \sigma + j\omega$	LaPlace Variable	rad/s
R	resistance	ohm
L	inductance	H
T	torque	n-m
J	inertia	kg-m ²
i	current	A
v	voltage	V
e	induced voltage (emf)	V
P	number of Poles	none
L	LaPlace operator	
L^{-1}	Inverse LaPlace operator	

1 INTRODUCTION

The recent advances in high power semiconductor switching devices, magnetic materials, and energy storage systems have generated considerable interest in electric drive systems for vehicle propulsion applications. Electric drive systems for propulsion can eliminate the need for shafts and gearing while increasing vehicle stealth and flexibility. Novel propulsion configurations and control strategies are pushing the need for high power density, high performance electric machines to operate in the harsh environments present in many electric drive applications.

The permanent magnet synchronous motor (PMSM) offers several features that make it attractive for use in electric drive systems. The PMSM offers increased power density, efficiency, and excellent acoustic performance when compared to induction and DC motors. In order to fully exploit the characteristics of the PMSM, high-resolution rotor angle information is required. This requirement originates from the need to effectively perform torque control on the PMSM. Furthermore, for speed control applications, the speed feedback is also required. A resolver or encoder attached to the shaft of the machine usually provides both the position and speed feedback. Many applications, however, cannot tolerate the use of such a position sensor. Thus, there has been an intense interest in the development of the *sensorless drive*, where the PMSM stator itself is used as the rotor position sensor.

1.1 Statement of Problem

Along with the recent interest in the PMSM by both military and industry came the development of new control techniques for current and direct torque control [2, 3], efficiency maximization [4], and torque ripple minimization [5, 6, 7, 8]. Each of these control techniques require accurate knowledge of the rotor angle in order to be effective. At the same time, new motor propulsion topologies such as integrated motor/propulsors that place the motor directly in a submerged environment [9] are initiating the need to eliminate these rotor position sensors. The requirement for high resolution rotor position information coupled with the unreliability of the rotor position transducers in an underwater environment has created a need for a rotor position *sensorless* strategy suitable for such propulsion applications. Thus, the development of a sensorless drive strategy for the PMSM is an enabling technology toward the successful implementation of the integrated motor/propulsor. The elimination of the high resolution rotor position sensor enhances the value of using the PMSM in many other Navy applications as well due to space and weight savings that translate to additional payload volume and increased reliability.

1.2 Statement of Purpose

In this document, the implementation of a sensorless PMSM drive is presented. The hardware implementation is detailed, implementation issues are discussed, and

experimental results are used to verify the effectiveness of the developed system. Through experimentation, the developed sensorless strategy will be shown to result in Naval electric drive capabilities that fully utilize many of the attractive characteristics of the PMSM without the requirement for a high resolution position sensor.

1.3 Organization of Report

This document focuses on the implementation of a sensorless electric drive for a high-power PMSM. In Chapter 2, a cursory review of the rotor position estimation technique developed in [1] is presented. To complement this original development, a rotor angle estimation error analysis is performed to quantify the effects of PMSM model uncertainty.

In Chapter 3, the hardware implementation of the rotor position estimation technique is presented. The details of the hardware implementation are shown in detail, and implementation issues are discussed. The performance of the resulting sensorless drive is examined through the extensive real-time experiments in Chapter 4. Finally, conclusions of the research and remaining issues are set forth in Chapter 5.

2 ROTOR POSITION ESTIMATION

In this section, a review of a model-based rotor position estimator developed in [1] is presented. From this proposed rotor position estimator model, rotor angle estimation error analysis is performed so that the effects of PMSM model uncertainty and measurement errors can be quantified.

2.1 Sensorless PMSM Model

The flux linkage model of the non-salient PMSM in the two-phase stationary reference frame [10] is:

$$\frac{d}{dt} \begin{bmatrix} \lambda_\alpha \\ \lambda_\beta \end{bmatrix} = \begin{bmatrix} v_\alpha \\ v_\beta \end{bmatrix} - \tau \left(\begin{bmatrix} \lambda_\alpha \\ \lambda_\beta \end{bmatrix} - \begin{bmatrix} \lambda_{pm\alpha} \\ \lambda_{pm\beta} \end{bmatrix} \right), \quad (1)$$

where

$$\tau = \frac{R}{\frac{3}{2}L_{av}}; \quad \begin{bmatrix} \lambda_{pm\alpha} \\ \lambda_{pm\beta} \end{bmatrix} = \sqrt{\frac{3}{2}}\lambda_m \begin{bmatrix} \cos\theta \\ \sin\theta \end{bmatrix}. \quad (2)$$

The terms $\lambda_{\alpha,\beta}$ and $v_{\alpha,\beta}$ represent the flux linkages and voltages corresponding to the two fictitious windings in the stationary reference frame. The symbols L_{av} , λ_m , R , and

θ represent the self inductance, PM flux constant, resistance, and rotor angle, respectively.

To develop a model for a rotor position observer, the vector $[\lambda_{pma} \ \lambda_{pm\beta}]^T$ defined in (2) is considered to be a disturbance state that satisfies a known differential equation. Combining the disturbance state vector with the state variables defined in (1) yields the metastate vector, \mathbf{x} :

$$\mathbf{x} = [x_1 \ x_2 \ x_3 \ x_4]^T = [\lambda_\alpha \ \lambda_\beta \ \lambda_{pma} \ \lambda_{pm\beta}]^T. \quad (3)$$

The input vector is the applied phase voltage in the stationary two-phase reference frame

$$\mathbf{u} = [u_1 \ u_2]^T = [v_\alpha \ v_\beta]^T, \quad (4)$$

and the output vector, \mathbf{y} , is chosen to be the measurable currents:

$$\mathbf{y} = [y_1 \ y_2]^T = [i_\alpha \ i_\beta]^T. \quad (5)$$

Thus, the metasystem state and output equations are described by

$$\dot{\mathbf{x}} = \mathbf{A}_\omega \mathbf{x} + \mathbf{B} \mathbf{u} \quad (6)$$

$$\mathbf{y} = \mathbf{C} \mathbf{x}, \quad (7)$$

respectively, where

$$\mathbf{A}_\omega = \begin{bmatrix} -\tau & 0 & \tau & 0 \\ 0 & -\tau & 0 & \tau \\ 0 & 0 & 0 & -\omega_e \\ 0 & 0 & \omega_e & 0 \end{bmatrix}; \quad \mathbf{B} = \begin{bmatrix} 1 & 0 \\ 0 & 1 \\ 0 & 0 \\ 0 & 0 \end{bmatrix} \quad (8)$$

$$\mathbf{C} = \begin{bmatrix} \frac{\tau}{R} & 0 & -\frac{\tau}{R} & 0 \\ 0 & \frac{\tau}{R} & 0 & -\frac{\tau}{R} \end{bmatrix}$$

The term ω_e represents the angular velocity of the rotor shaft in electrical radians per second. The subscript ω associated with the \mathbf{A}_ω matrix is used to indicate variation with the rotor angular velocity.

Under the assumption that rotor velocity is approximately constant over the system sampling period, the angular velocity may be considered to be a slowly varying PMSM parameter. This assumption is conservative given the large mechanical time constant relative to the fast electrical time constant of the typical PMSM propulsion motor. With this assumption, the resulting model is a linear time varying system, allowing the use of well-developed linear control methods. It is also stressed that the model given in (6) and (7) does not contain any mechanical variables such as torque, friction, and inertia in the state equations. This is advantageous, since torque and inertia are often unknown and vary during the operation of the system.

2.2 Rotor Position Observer

With angular velocity considered to be a slowly varying parameter, (6) and (7) may be used to construct a full order observer [11]. The observer is used to estimate the state vector \mathbf{x} of (3) from knowledge of the input vector \mathbf{u} and a direct measurement of the output vector \mathbf{y} . Note that from the estimation of x_3 and x_4 , the rotor position estimate $\hat{\theta}$ may be determined from

$$\hat{\theta} = \tan^{-1} \left(\frac{\hat{x}_4}{\hat{x}_3} \right). \quad (9)$$

Using standard observer design techniques for a linear system [12], the form of the proposed rotor position observer is

$$\dot{\mathbf{e}} = (\mathbf{A}_\omega - \mathbf{GC})\mathbf{e} \quad (10)$$

where \mathbf{e} is the state estimation error vector

$$\mathbf{e} = \mathbf{x} - \hat{\mathbf{x}}, \quad (11)$$

\mathbf{G} is the observer gain matrix, and $\hat{\mathbf{x}}$ is the estimated state vector.

The convergence of the estimated state variables toward their actual values is achieved by conventional pole-placement techniques. The eigenvalues of the characteristic equation

$$|\lambda \mathbf{I} - (\mathbf{A}_\omega - \mathbf{GC})| = 0 \quad (12)$$

are chosen to have negative real components so that asymptotic state reconstruction is achieved.

Clearly, observability of the system is a requirement for the estimation of PMSM states. The condition for observability is determined by the rank of the observability matrix [13]:

$$\begin{bmatrix} \mathbf{C} & \mathbf{CA}_\omega & \mathbf{CA}_\omega^2 & \mathbf{CA}_\omega^3 \end{bmatrix}^T. \quad (13)$$

From (13), the system is observable for non-zero angular velocity. This result supports the well-known drawback of the sensorless PMSM – its inability to estimate rotor angle at zero and low angular velocities [14, 15].

Given the ill-conditioning of the rotor position observer at standstill, special provisions must be made to start the sensorless PMSM and to operate the system at extremely low angular velocity. For the sensorless drive demonstrator system, the observer feedback is disabled at speeds below 7.5 r/s (18 RPM), which represents an experimentally determined low-speed threshold.

2.3 Angular Velocity Estimation

It is clear from (8) that rotor velocity is a required parameter for the implementation of the proposed rotor position observer. In addition, angular velocity feedback is required to accurately track the velocity reference in a speed control loop used in most propulsion systems. Therefore, in the absence of an angular velocity sensor, a suitable strategy must be developed to determine this parameter. Two strategies are described in the following sections, and the strengths of each technique are combined to form an adaptive velocity estimation scheme.

2.3.1 Quasi Steady State Velocity Estimation

A quasi steady state estimate for magnitude of the angular velocity [16] is

$$|\hat{\omega}_e| = \frac{\sqrt{(v_\alpha - Ri_\alpha)^2 + (v_\beta - Ri_\beta)^2}}{\sqrt{3/2}\lambda_m}. \quad (14)$$

This result suggests the use of the input and output vectors, \mathbf{u} and \mathbf{y} , to estimate the magnitude of the angular velocity. The direction of the angular velocity estimate at sampling interval k is then obtained from

$$\hat{\omega}_e = \text{sgn}(\phi(k) - \phi(k-1))|\hat{\omega}_e|, \quad (15)$$

where

$$\phi(k) = \tan^{-1} \left(\frac{Ri_\alpha(k) - v_\alpha(k)}{v_\beta(k) - Ri_\beta(k)} \right). \quad (16)$$

The strength of this method is its ability to determine velocity – even at zero and very low speeds. The weakness is its dependency on PMSM parameters.

2.3.2 Time Derivative of Estimated Rotor Angle

An alternative to the method given in (15) is to use the time derivative of the estimated rotor angle

$$\hat{\omega}_e = d\hat{\theta}/dt. \quad (17)$$

This method obviously requires a stable position observer, and the observer pole locations should be much faster than the angular velocity. Both of these constraints may be enforced by proper selection of the system eigenvalues at non-zero angular velocity. Subject to these constraints, the estimated angular velocity obtained by (17) approaches the actual value when averaged over a sufficient period of time, as shown in [18].

The drawback to this method is the noise that results from the differentiation process and its inability to obtain an accurate speed estimate at startup, where the rotor position is not observable. The strength of this method is the accuracy of the steady state speed estimates throughout the medium to high speed range.

2.3.3 Adaptive Velocity Estimation

The two proposed velocity estimation methods complement each other nicely. The use of (15) yields good performance at very low speeds, but is subject to parameter uncertainty. The use of (17), however, is essentially independent of the parameter estimation errors so long as the system poles are chosen to be faster than the angular velocity and the velocity is sampled over a sufficient period of time. Thus, the strengths of each method may be combined to form the velocity estimation correction scheme, as shown in Figure 1.

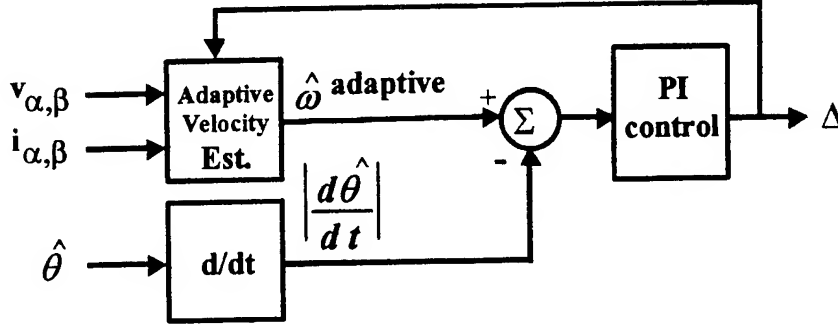


Figure 1. Velocity estimation correction block.

To use (17) to correct for velocity estimation errors obtained by (15), (14) is modified to include an uncertainty term Δ , which represents the uncertainty in the permanent magnet flux linkage:

$$|\hat{\omega}_e| = \frac{\sqrt{(v_\alpha - Ri_\alpha)^2 + (v_\beta - Ri_\beta)^2}}{\sqrt{\frac{3}{2}}(\lambda_m + \Delta)}. \quad (18)$$

Initially, the error term Δ is set to zero. However, as long as the magnitude of the estimated velocity is above the low speed threshold where the position observer is assumed to be stable, the adaptive velocity estimation process is activated.

The adaptation process compares the output of (18) with (17) to generate the velocity estimation error. A PI controller operates on the estimation error, adjusting the output Δ to correct for the parameter uncertainty. The time constant of the PI controller is chosen to be slow, since the temperature effect that causes the parameter drift is a very slow effect as well. This has the benefit that the noise generated by the differentiation of the rotor angle estimate is smoothed over time. Thus, as long as the rotor position estimator remains stable, the average value of its derivative is close to the actual rotor speed.

This velocity estimation scheme has been shown through experimentation [17] to produce accurate tracking of the velocity reference, despite the absence of the position/velocity sensor. This is of critical importance in undersea vehicles where the rotor angular velocity is used to achieve the desired forward vehicle speed. An overall block diagram of the proposed position observer, including the angular velocity estimation block, is shown in Figure 2.

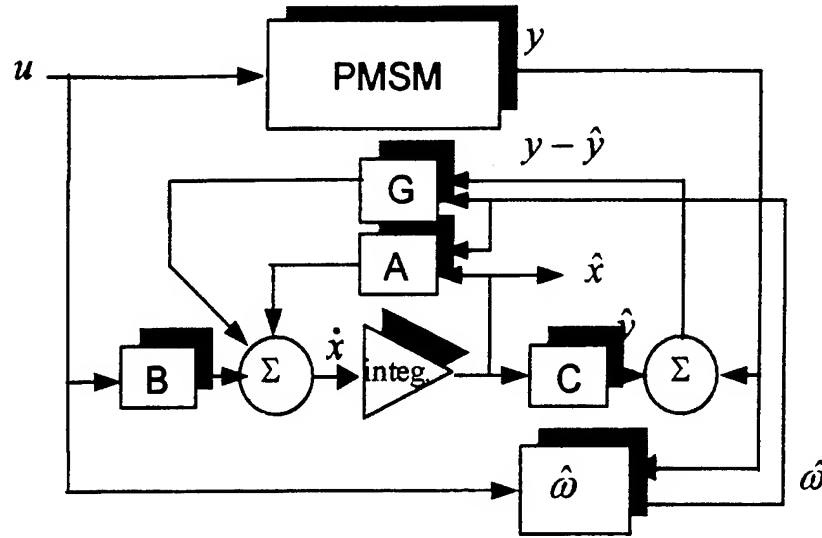


Figure 2. Block diagram of rotor position estimator.

2.4 Rotor Position Observer Pole Placement

From the system model given in (6), the open-loop eigenvalues λ_{PMSM} of the plant (PMSM) are

$$\begin{aligned} \lambda_{PMSM1}, \lambda_{PMSM2} &= -\tau \\ \lambda_{PMSM3}, \lambda_{PMSM4} &= \pm j\omega_e \end{aligned} \quad (19)$$

In general, the location of the desired observer eigenvalues λ can be represented by their locations on the real (Re) and imaginary (Im) axis:

$$\begin{aligned} \lambda_1 &= Re_1 + jIm_1 ; \lambda_2 = \lambda_1^* = Re_1 - jIm_1 \\ \lambda_3 &= Re_2 + jIm_2 ; \lambda_4 = \lambda_3^* = Re_2 - jIm_2 \end{aligned} \quad (20)$$

The system eigenvalues are moved from their open-loop locations (19) to the desired locations (20) through the selection of the observer gain matrix G in (10). It is the observer eigenvalue locations that determine the rate of convergence of the angle estimate error towards zero and the stability of the observer. In this section, the relation between the observer gain matrix, the operating condition of the PMSM, and the desired eigenvalues is presented.

It will be shown later that it is advantageous to select the eigenvalues of the observer such that their magnitude is much greater than the PMSM angular velocity. Therefore, the observer eigenvalues are placed according to the angular speed of the rotor ω_e :

$$\begin{aligned}\lambda_1 = \lambda_3 &= |\omega_e|(-k_{\lambda-real} + jk_{\lambda-imag}) \\ \lambda_2 = \lambda_4 = \lambda_1^* &= |\omega_e|(-k_{\lambda-real} - jk_{\lambda-imag})\end{aligned}\quad (21)$$

where $k_{\lambda-real}$ and $k_{\lambda-imag}$ define the response and damping characteristics of the observer. In practice, the eigenvalues of the position observer should always be selected such that the position estimation error converges at a fast rate with respect to the rotor angular velocity. Therefore, in the experimental system, $k_{\lambda-real}$ was selected so that the observer poles were at least four times faster than the rotor velocity – that is $k_{\lambda-real} \geq 4$. The imaginary pole placement constant $k_{\lambda-imag}$ was selected to be approximately half of $k_{\lambda-real}$, which was found to produce good damping characteristics. Therefore, from (21), the gain scheduler in the prototype sensorless PMSM drive selects the observer gain values based on the estimated rotor velocity.

Each time a new velocity estimate is available, the observer gain matrix G is updated by using conventional pole-placement methods. With this technique, the eigenvalues of the characteristic equation

$$|\lambda I - (A_o - GC)| = 0 \quad (22)$$

are placed in the left-half plane at the locations specified by (21) so that the observer estimation error e converges to zero within a satisfactory period of time. In [18], a solution to (22) is developed, and the observer gain matrix G required to place the eigenvalues at the location specified by (21) is found to be:

$$G = \begin{bmatrix} -R & -\frac{R\lambda_1\lambda_2}{\omega_e\tau} \\ \frac{R\lambda_1\lambda_2}{\omega_e\tau} & -R \\ \frac{R(\lambda_1 + \lambda_2)}{\tau} & \frac{R(-\lambda_1\lambda_2 + \omega_e^2)}{\omega_e\tau} \\ -\frac{R(-\lambda_1\lambda_2 + \omega_e^2)}{\omega_e\tau} & \frac{R(\lambda_1 + \lambda_2)}{\tau} \end{bmatrix} \quad (23)$$

Note that the observer gain matrix G is dependent on the rotor velocity, the desired eigenvalue locations, and the PMSM stator winding parameters. In practice, since velocity is estimated in a sensorless system, the gain matrix G is calculated using $\hat{\omega}_e$ instead of using ω_e as indicated in (23).

2.5 Estimation Error Analysis

The error dynamics of the state estimator given by (10) for the full-order observer shows that asymptotic state reconstruction is achieved if the eigenvalues of $\mathbf{A}_o - \mathbf{G}\mathbf{C}$ have negative reals. For parameter uncertainty, the system matrix of the plant and reference model differ, resulting in state reconstruction error. In this section, the effects of such parameter uncertainties on the rotor position estimator accuracy are investigated.

To quantify the effect of parameter uncertainties on rotor angle estimation accuracy, (9) is used with (11) to reveal the relation between the rotor angle estimation error and the error associated with estimated states \hat{x}_3 and \hat{x}_4 :

$$\hat{\theta} = \tan^{-1} \left(\frac{x_4 - e_4}{x_3 - e_3} \right) = \tan^{-1} \left(\frac{\lambda_{pm\beta} - e_4}{\lambda_{pm\alpha} - e_3} \right) \quad (24)$$

For the convenience of graphical representation (24) can be expressed as a space phasor:

$$Ke^{j\hat{\theta}} = j(\lambda_{pm\beta} - e_4) + (\lambda_{pm\alpha} - e_3) , \quad (25)$$

where K is the amplitude of the rotating phasor. This is shown graphically in Figure 3, which clearly shows how state estimation errors e_3 and e_4 result in a difference between the actual and estimated rotor angles – shown as θ and $\hat{\theta}$, respectively.

In the event of zero estimation error, (24) shows that the estimation error is equal to the actual angle since

$$\hat{\theta} = \tan^{-1} \left(\frac{\sqrt{3/2}\lambda_m \sin \theta}{\sqrt{3/2}\lambda_m \cos \theta} \right) = \theta . \quad (26)$$

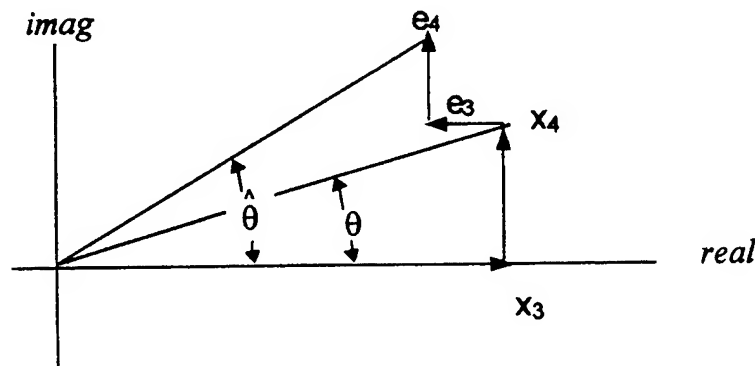


Figure 3. Effect of state estimation error on angle estimation.

In this case, the space phasor defined by (25) is defined in steady state by a circle of radius $\lambda_{pma,\beta}$ centered on the origin. In the case of nonzero state estimation error, however, the trajectory traced by the space phasor of (25) is no longer defined by a circle centered at the origin. The trajectory of this space phasor is a convenient graphical tool with which to characterize the rotor angle estimation error, and will be used in the following sections with the goal of characterizing the effects of parameter uncertainties on the rotor angle estimation accuracy.

2.5.1 Effect of Angular Velocity Estimation on Rotor Angle Estimation Accuracy

For a shaft sensorless PMSM drive, rotor velocity must be estimated as well as the rotor position. It follows that the slowly varying velocity ω_e and its estimated value $\hat{\omega}_e$ are related by

$$\omega_e = \hat{\omega}_e + \Delta\omega_e, \quad (27)$$

where $\Delta\omega_e$ is the velocity estimation error. From the state model of (6), where A_ω is velocity dependent, the plant behavior can be expressed with respect to the estimated velocity and the corresponding velocity estimation error:

$$\dot{\mathbf{x}} = \mathbf{A}_{\hat{\omega}} \mathbf{x} + \mathbf{A}_{\Delta\omega} \mathbf{x} + \mathbf{B} \mathbf{u}, \quad (28)$$

where

$$\mathbf{A}_{\hat{\omega}} = \begin{bmatrix} -\tau & 0 & \tau & 0 \\ 0 & -\tau & 0 & \tau \\ 0 & 0 & 0 & -\hat{\omega}_e \\ 0 & 0 & \hat{\omega}_e & 0 \end{bmatrix}; \quad \mathbf{A}_{\Delta\omega} = \begin{bmatrix} 0 & 0 & 0 & 0 \\ 0 & 0 & 0 & 0 \\ 0 & 0 & 0 & -\Delta\omega_e \\ 0 & 0 & \Delta\omega_e & 0 \end{bmatrix}. \quad (29)$$

Similarly, the reference model will behave according to

$$\dot{\hat{\mathbf{x}}} = \mathbf{A}_{\hat{\omega}} \hat{\mathbf{x}} + \mathbf{B} \mathbf{u} + \mathbf{G} \mathbf{C} (\mathbf{x} - \hat{\mathbf{x}}). \quad (30)$$

From the state estimation error given in (11),

$$\dot{\mathbf{e}} = \dot{\mathbf{x}} - \dot{\hat{\mathbf{x}}}. \quad (31)$$

so that from (28) and (30), the error dynamics with uncertainty in the angular velocity become

$$\dot{\mathbf{e}} = (\mathbf{A}_{\hat{\omega}} - \mathbf{G} \mathbf{C}) \mathbf{e} + \mathbf{A}_{\Delta\omega} \mathbf{x}. \quad (32)$$

In order for the errors in (32) go to zero asymptotically, independent of \mathbf{x} , the coefficient of \mathbf{x} would have to be zero and $\mathbf{A}_{\hat{\omega}} - \mathbf{G}\mathbf{C}$ must be the dynamics matrix of a stable system. When these conditions are met, the error dynamics are reduced to the homogeneous equation, and the error approaches zero in steady state. In practice, the requirement for zero angular velocity estimation error is a difficult objective and therefore an analysis of velocity uncertainty on angle estimation accuracy is required.

In order to quantify the effects of the velocity estimation error on rotor position estimation accuracy, (32) is solved to reveal the steady state estimation error corresponding to estimated states \hat{x}_3 and \hat{x}_4 :

$$\begin{bmatrix} e_{3,\Delta\omega}(t) \\ e_{4,\Delta\omega}(t) \end{bmatrix} = \frac{\Delta\omega_e}{\hat{\omega}_e} \sqrt{\frac{3}{2}} \lambda_m K_\lambda \begin{bmatrix} \sin(\theta(t) + \phi) \\ -\cos(\theta(t) + \phi) \end{bmatrix}, \quad (33)$$

where

$$K_\lambda = \frac{\omega_e \hat{\omega}_e + \lambda_1 \lambda_2}{\sqrt{(\omega_e^2 + \lambda_1^2)(\omega_e^2 + \lambda_2^2)}}; \quad \phi = \tan^{-1} \left(\frac{\omega_e^2 - \lambda_1 \lambda_2}{\omega_e (\lambda_1 + \lambda_2)} \right). \quad (34)$$

The computational details of this result are included in [18]. Now, the estimated states with velocity estimation uncertainty can be written in terms of the estimated error:

$$\begin{aligned} \hat{x}_3 &= \sqrt{\frac{3}{2}} \lambda_m \cos \hat{\theta}(t) = \sqrt{\frac{3}{2}} \lambda_m \left(\cos \theta(t) - \frac{\Delta\omega_e}{\hat{\omega}_e} K_\lambda \sin(\theta(t) + \phi) \right) \\ \hat{x}_4 &= \sqrt{\frac{3}{2}} \lambda_m \sin \hat{\theta}(t) = \sqrt{\frac{3}{2}} \lambda_m \left(\sin \theta(t) + \frac{\Delta\omega_e}{\hat{\omega}_e} K_\lambda \cos(\theta(t) + \phi) \right) \end{aligned} \quad (35)$$

which through some trigonometric manipulations can be expressed by:

$$\begin{aligned} \begin{bmatrix} \hat{x}_3 \\ \hat{x}_4 \end{bmatrix} &= \sqrt{\frac{3}{2}} \lambda_m M \begin{bmatrix} \cos(\theta(t) + \delta) \\ \sin(\theta(t) + \delta) \end{bmatrix} \\ M &= \sqrt{\left(\frac{\Delta\omega_e}{\hat{\omega}_e} K_\lambda \cos \phi \right)^2 + \left(1 - \frac{\Delta\omega_e}{\hat{\omega}_e} K_\lambda \sin \phi \right)^2} \\ \delta &= \tan^{-1} \left(\frac{\frac{\Delta\omega_e}{\hat{\omega}_e} K_\lambda \cos \phi}{1 - \frac{\Delta\omega_e}{\hat{\omega}_e} K_\lambda \sin \phi} \right) \end{aligned} \quad (36)$$

Substitution of (36) into (9) reveals the effect of the velocity estimation error on position estimation accuracy:

$$\hat{\theta}(t) = \tan^{-1} \left(\frac{\sqrt{3/2} \lambda_m M \sin(\theta(t) + \delta)}{\sqrt{3/2} \lambda_m M \cos(\theta(t) + \delta)} \right) = \theta(t) + \delta \quad , \quad (37)$$

where δ is the position estimation error that results from angular velocity uncertainty. This result implies that for a given observer gain G , the position estimation accuracy is bound by the accuracy of the velocity estimation. Furthermore, it demonstrates that selection of the system eigenvalues such that $|\lambda_1, \lambda_2| \gg |\omega_e|$ (i.e., choose $k_{\lambda-real}$ and $k_{\lambda-imag}$ in (21) to be much greater than one) reduces the effects of velocity estimation error by forcing $\phi \rightarrow -\pi/2$, so that $\delta \rightarrow 0$.

Figure 4 shows the locus of the estimated state and angle estimation error resulting from a $\pm 10\%$ velocity estimation error and positive angular velocity. To accentuate the angle estimation error, the closed-loop eigenvalue reals were approximately equal to the angular velocity. In Figure 4, δ is the angle between a line drawn from the origin to the point on the locus marked $\theta = 0$ and the x_3 axis on the locus plots, or the vertical distance $\hat{\theta} - \theta$ in the plots showing actual and estimated angles. The estimated angle leads and lags the actual angle for negative and positive velocity estimation errors, respectively.

The effect of moving the pole locations further into the left half plane is shown in Figure 5. Increasing the magnitude of the conjugate pair λ_1, λ_2 drives the angle ϕ toward $-\pi/2$ and δ toward zero. Figure 5 represents the same operating condition as the second column in Figure 4, but in comparison has much lower angle estimation error due to the pole locations.

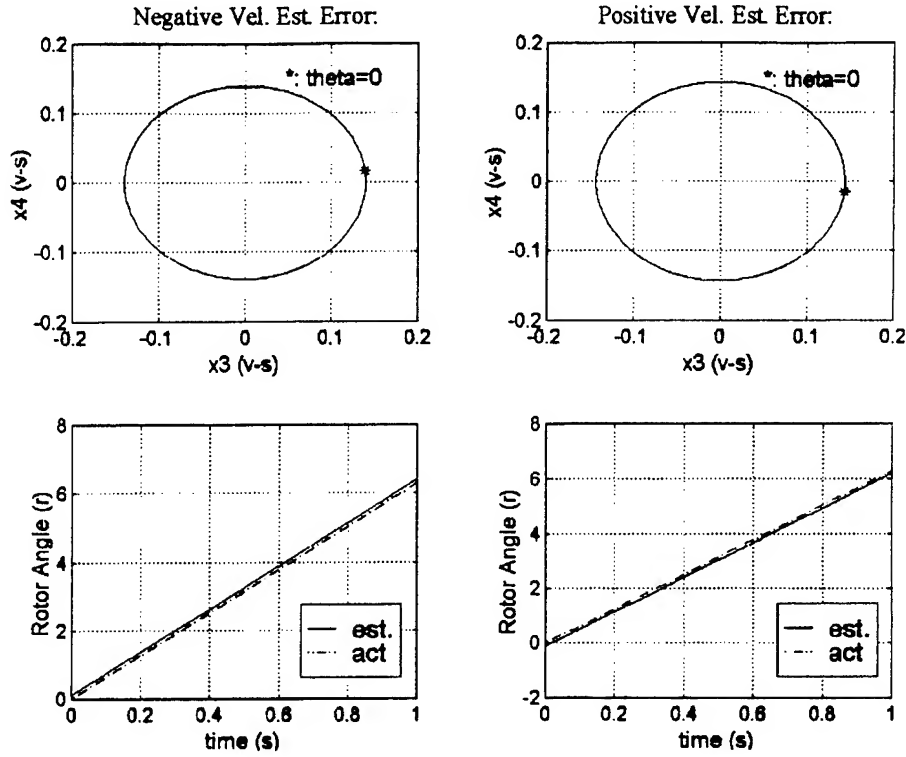


Figure 4. Angle estimation error due to $\pm 10\%$ velocity error, slow observer poles.

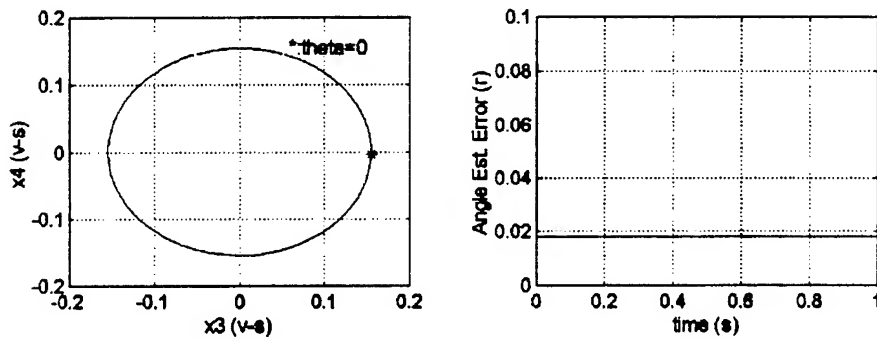


Figure 5. Angle estimation with 10 percent velocity error, fast observer poles.

2.5.2 Effect of Stator Resistance Uncertainty on Angle Estimation Accuracy

In the PMSM, the most temperature sensitive parameter is the stator winding resistance, which varies linearly over the operating temperature of the machine [19]. It is therefore reasonable to assume that the angle estimation process will be subject to uncertainty in this parameter, and a study of its effect is crucial.

The relation between the actual stator resistance and the nominal value used by the reference model can be represented by

$$R = \hat{R} + \Delta R \quad , \quad (38)$$

where \hat{R} is the stator resistance value used by the PMSM internal model, R is the actual PMSM stator resistance, and ΔR represents the modeling error. By using (38) and assuming that all other parameters are accurately known, the PMSM system matrix given in (8) can be expanded to reflect the resistance uncertainty:

$$\mathbf{A}_\omega = \hat{\mathbf{A}}_\omega + \mathbf{A}_{\Delta R} = \begin{bmatrix} -\frac{\hat{R}}{L_s} & 0 & \frac{\hat{R}}{L_s} & 0 \\ 0 & -\frac{\hat{R}}{L_s} & 0 & \frac{\hat{R}}{L_s} \\ 0 & 0 & 0 & -\omega_e \\ 0 & 0 & \omega_e & 0 \end{bmatrix} + \begin{bmatrix} -\frac{\Delta R}{L_s} & 0 & \frac{\Delta R}{L_s} & 0 \\ 0 & -\frac{\Delta R}{L_s} & 0 & \frac{\Delta R}{L_s} \\ 0 & 0 & 0 & 0 \\ 0 & 0 & 0 & 0 \end{bmatrix} . \quad (39)$$

Thus, the PMSM and reference model behave according to

$$\dot{\mathbf{x}} = \hat{\mathbf{A}}_\omega \mathbf{x} + \mathbf{A}_{\Delta R} \mathbf{x} + \mathbf{B} \mathbf{u} \quad , \quad (40)$$

$$\dot{\hat{\mathbf{x}}} = \hat{\mathbf{A}}_\omega \hat{\mathbf{x}} + \mathbf{B} \mathbf{u} + \mathbf{G} \mathbf{C}(\mathbf{x} - \hat{\mathbf{x}})$$

respectively, so the error dynamics defined in (31) become

$$\dot{\mathbf{e}} = \dot{\mathbf{x}} - \dot{\hat{\mathbf{x}}} = (\hat{\mathbf{A}}_\omega - \mathbf{G} \mathbf{C}) \mathbf{e} + \mathbf{A}_{\Delta R} \mathbf{x} . \quad (41)$$

The solution to (41) from [18] reveals the steady state estimation errors introduced in the states \hat{x}_3 and \hat{x}_4 due to resistance uncertainty:

$$\begin{bmatrix} e_{3,\Delta R} \\ e_{4,\Delta R} \end{bmatrix} = \frac{\Delta R}{\omega_e L_s} \begin{bmatrix} -\lambda_p \sin(\theta + \varepsilon) + \sqrt{\frac{3}{2}} \lambda_m \sin \omega_e t \\ \lambda_p \cos(\theta + \varepsilon) - \sqrt{\frac{3}{2}} \lambda_m \cos \omega_e t \end{bmatrix} . \quad (42)$$

In (42), the angle ε represents the angle between the resultant stator flux and the flux generated by the rotor permanent magnets alone. For the lightly loaded or low-inductance PMSM such as a slotless design, this angle will be approximately zero. For a smaller airgap machine, the angle ε will increase with stator current.

From the state estimation error in (42), the effects on the rotor angle estimation accuracy due to resistance uncertainty are determined from (9), (11), and (42):

$$\hat{\theta}(t) = \tan^{-1} \left(\frac{x_4 - e_{4,\Delta R}}{x_3 - e_{3,\Delta R}} \right) = \tan^{-1} \left(\frac{\sqrt{\frac{3}{2}} \lambda_m \sin \theta(t) - e_{4,\Delta R}}{\sqrt{\frac{3}{2}} \lambda_m \cos \theta(t) - e_{3,\Delta R}} \right). \quad (43)$$

Substitution of (42) into (43), and the trigonometric manipulations detailed in Appendix B of [18] yields the angle estimation error induced by resistance uncertainty:

$$\begin{aligned} \hat{\theta}_{\Delta R} &= \tan^{-1} \left(\frac{\sin(\theta + \delta_R)}{\cos(\theta + \delta_R)} \right) = \theta + \delta_R \\ \delta_R &= \tan^{-1} \left(\frac{\Delta R}{\omega_e} \frac{(I_m \sin \xi)}{\left(\sqrt{\frac{3}{2}} \lambda_m + \frac{\Delta R I_m}{\omega_e} \cos \xi \right)} \right), \end{aligned} \quad (44)$$

where ξ represents the angle of the stator current with respect to the generated emf. From the result of (44), the effect of stator resistance uncertainty is to introduce a steady rotor angle estimation error of δ_R , whose magnitude is proportional to the resistance uncertainty and inversely proportional to angular velocity. The error is shown in Figure 6, where δ_R is the angle between the x_3 axis and a line drawn from the origin to the point on the locus marked $\theta = 0$. In the simulation shown in Figure 6, the nominal resistance is $1.35 \, \Omega$ while the actual stator resistance due to heating is $2.35 \, \Omega$. Angular velocity is $100 \, \text{r/s}$, and the machine is assumed to be operating such that an angle of $\xi = -\pi/10$ is present between the back emf and the stator currents.

In the above error analysis, it was assumed that the resistance uncertainty is balanced. In the event of unbalanced resistance error, the locus shown in Figure 6 is deflected into an oval shape. The non-circular locus of the estimated states results in an additional angle estimation error at twice the fundamental frequency in addition to the constant angle error term δ_R .

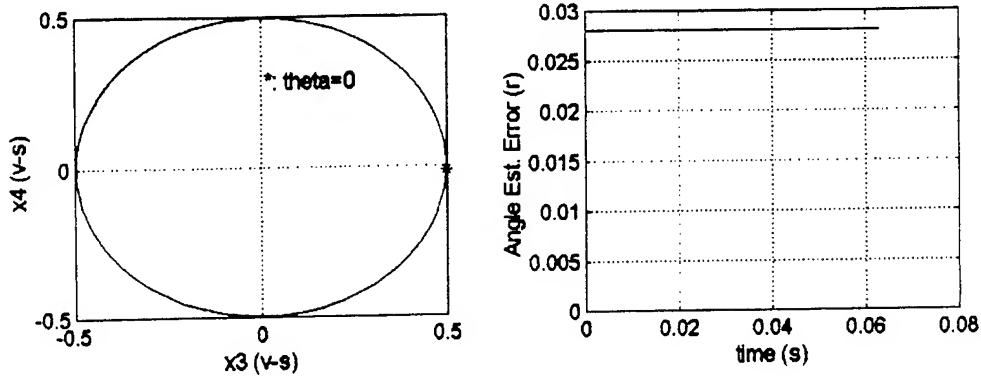


Figure 6. Resistance uncertainty effect on angle estimation: $\Delta R = 1\Omega$, heavily loaded.

In the expression for δ_R , the numerator is seen to be dependent on the magnitude of the stator current. In the extreme case of zero stator current, the numerator goes to zero and no angle estimation errors result from resistance uncertainty. This is an easily justifiable result, since angle estimation of an open circuit stator PMSM does not require knowledge of the stator resistance. It should also be noted that if the stator current is in phase with the back emf (i.e. $\xi = 0$), uncertainty in the stator resistance generates no error in the estimated rotor angle.

2.5.3 Effect of Stator Inductance Uncertainty on Angle Estimation Accuracy

In the event that the stator inductance is not known accurately, an angle estimation error will result. The characteristics of the angle estimation error due to inductive uncertainty are now analyzed by representing the actual stator inductance as

$$L_s = \hat{L}_s + \Delta L, \quad (45)$$

where L_s , \hat{L}_s , and ΔL are the actual value, estimated value, and uncertainty of the stator inductance, $L_s = L_l + \frac{3}{2}L_{\sigma}$. Given the inductance uncertainty defined in (45), the PMSM dynamics may be described by

$$\dot{\mathbf{x}} = \hat{\mathbf{A}}_{\omega} \mathbf{x} + \mathbf{A}_{\Delta L} \mathbf{x} + \mathbf{B} \mathbf{u}, \quad (46)$$

where the actual system matrix given in (8) is expanded to include the inductance uncertainty term:

$$\mathbf{A}_\omega = \hat{\mathbf{A}}_\omega + \mathbf{A}_{\Delta L} = \begin{bmatrix} -\frac{R}{\hat{L}_s + \Delta L} & 0 & \frac{R}{\hat{L}_s + \Delta L} & 0 \\ 0 & -\frac{R}{\hat{L}_s + \Delta L} & 0 & \frac{R}{\hat{L}_s + \Delta L} \\ 0 & 0 & 0 & -\omega_e \\ 0 & 0 & \omega_e & 0 \end{bmatrix}. \quad (47)$$

The system matrix used by the PMSM reference model and the corresponding uncertainty in the system matrix due to inductance error matrix in this case are described by

$$\hat{\mathbf{A}}_\omega = \begin{bmatrix} -\frac{R}{\hat{L}_s} & 0 & \frac{R}{\hat{L}_s} & 0 \\ 0 & -\frac{R}{\hat{L}_s} & 0 & \frac{R}{\hat{L}_s} \\ 0 & 0 & 0 & -\omega_e \\ 0 & 0 & \omega_e & 0 \end{bmatrix}, \quad (48)$$

$$\mathbf{A}_{\Delta L} = \begin{bmatrix} \frac{R\Delta L}{\hat{L}_s(\hat{L}_s + \Delta L)} & 0 & -\frac{R\Delta L}{\hat{L}_s(\hat{L}_s + \Delta L)} & 0 \\ 0 & \frac{R\Delta L}{\hat{L}_s(\hat{L}_s + \Delta L)} & 0 & -\frac{R\Delta L}{\hat{L}_s(\hat{L}_s + \Delta L)} \\ 0 & 0 & 0 & 0 \\ 0 & 0 & 0 & 0 \end{bmatrix}$$

respectively.

In addition, the inductance error also appears in the output matrix \mathbf{C} defined in (8). To include this effect, the PMSM output matrix defined in (8) can be rewritten to account for the uncertainty in the stator inductance:

$$\mathbf{C} = \hat{\mathbf{C}} + \mathbf{C}_{\Delta L} = \begin{bmatrix} \frac{1}{\hat{L}_s + \Delta L} & 0 & -\frac{1}{\hat{L}_s + \Delta L} & 0 \\ 0 & \frac{1}{\hat{L}_s + \Delta L} & 0 & -\frac{1}{\hat{L}_s + \Delta L} \end{bmatrix}, \quad (49)$$

where the output matrix used by the reference model is

$$\hat{\mathbf{C}} = \begin{bmatrix} \frac{1}{\hat{L}_s} & 0 & -\frac{1}{\hat{L}_s} & 0 \\ 0 & \frac{1}{\hat{L}_s} & 0 & -\frac{1}{\hat{L}_s} \end{bmatrix}, \quad (50)$$

and the error in the output matrix created due to the uncertainty in the inductance is

$$\mathbf{C}_{\Delta L} = \begin{bmatrix} -\frac{\Delta L}{\hat{L}_s(\hat{L}_s + \Delta L)} & 0 & \frac{\Delta L}{\hat{L}_s(\hat{L}_s + \Delta L)} & 0 \\ 0 & -\frac{\Delta L}{\hat{L}_s(\hat{L}_s + \Delta L)} & 0 & \frac{\Delta L}{\hat{L}_s(\hat{L}_s + \Delta L)} \end{bmatrix}. \quad (51)$$

The PMSM reference model dynamics, in the case of inductance uncertainty, are

$$\dot{\hat{\mathbf{x}}} = \hat{\mathbf{A}}_{\omega} \hat{\mathbf{x}} + \mathbf{B}\mathbf{u} + \mathbf{G}\{(\hat{\mathbf{C}} + \mathbf{C}_{\Delta L})\hat{\mathbf{x}} - \hat{\mathbf{C}}\hat{\mathbf{x}}\}, \quad (52)$$

and finally, the error dynamics are determined from (46) and (52) are

$$\dot{\mathbf{e}} = \dot{\mathbf{x}} - \dot{\hat{\mathbf{x}}} = (\hat{\mathbf{A}}_{\omega} - \mathbf{G}\hat{\mathbf{C}})\mathbf{e} + (\mathbf{A}_{\Delta L} - \mathbf{G}\mathbf{C}_{\Delta L})\hat{\mathbf{x}}. \quad (53)$$

From Appendix B of [18], the steady state solution to (53) is

$$\begin{bmatrix} e_{3,\Delta L} \\ e_{4,\Delta L} \end{bmatrix} = \frac{\Delta L}{L_s} \begin{bmatrix} -\lambda_p \cos(\theta + \varepsilon) + \sqrt{\frac{3}{2}}\lambda_m \cos\theta(t) \\ -\lambda_p \sin(\theta + \varepsilon) + \sqrt{\frac{3}{2}}\lambda_m \sin\theta(t) \end{bmatrix}. \quad (54)$$

The effects of the state estimation error caused by inductance modeling uncertainty may be related to angle estimation accuracy by (9) and (11). In Appendix B of [18], it is shown that the estimated state variables can be written as

$$\begin{aligned} \hat{x}_3 &= \sqrt{\frac{3}{2}}\lambda_m \cos\theta(t) - e_3 = \sqrt{e^2 + d^2} \cos(\theta + \delta_L) \\ \hat{x}_4 &= \sqrt{\frac{3}{2}}\lambda_m \sin\theta(t) - e_4 = \sqrt{e^2 + d^2} \sin(\theta + \delta_L) \end{aligned}, \quad (55)$$

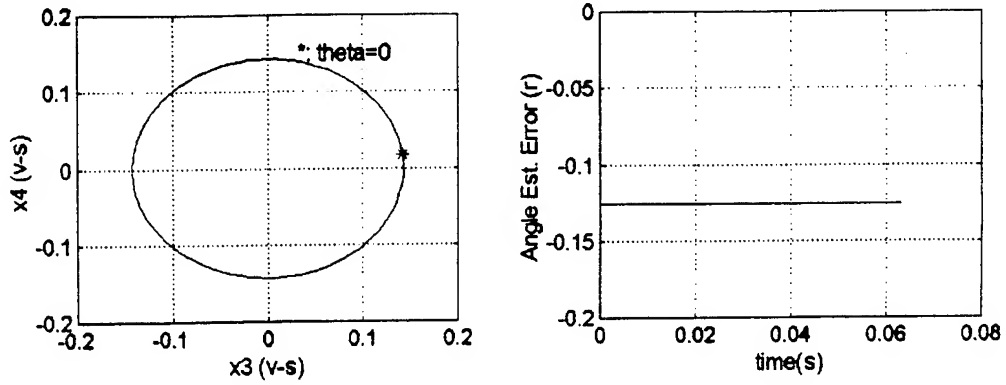


Figure 7. Stator inductance uncertainty effect on rotor angle estimation.

where

$$e = \Delta L I_m \cos \xi ; d = \sqrt{\frac{3}{2}} \lambda_m - \Delta L I_m \sin \xi$$

$$\delta_L = \tan^{-1} \left(\frac{e}{d} \right) = \tan^{-1} \left(\frac{\Delta L I_m \cos \xi}{\sqrt{\frac{3}{2}} \lambda_m - \Delta L I_m \sin \xi} \right) . \quad (56)$$

From this result, inductance error introduces a constant angle estimation error δ_L , whose amplitude is proportional to the magnitude of the inductance uncertainty, the stator current amplitude, and the angle ξ of the stator current with respect to the generated emf. The result of inductance uncertainty is shown in the locus of Figure 7, where the offset δ_L is illustrated by the angle between the x_3 axis and a line drawn from the origin to the point marked as $\theta = 0$. In the event of unbalanced inductance uncertainty, the locus in Figure 7 is distorted such that an additional double frequency term is added to the constant estimation error δ_L .

2.5.4 Effect of PM Flux Linkage Uncertainty on Angle Estimation Accuracy

Although the PM flux linkage constant is not a parameter in the PMSM reference model used for rotor angle estimation, it is required to estimate angular velocity when the slow mode approach is used. Therefore, when this method of velocity estimation is active, the effect of the permanent magnet flux linkage uncertainty can be considered to be the same

as a rotor velocity estimation error, since uncertainty in this parameter translates to uncertainty in the angular velocity.

2.5.5 Effect of Stator Voltage and Current Measurement Errors

The implementation of the rotor position observer requires the acquisition of the stator currents and voltages. The use of these signals in the rotor position estimator will result in estimation inaccuracy when the sensed quantities contain scaling or offset error. Furthermore, the inaccuracies may be unequal or unbalanced from one phase to another. The effects of these measurement inaccuracies are examined in this section.

2.5.5.1 Voltage Measurement Error

In the case of voltage sensing error, the actual and acquired signals are related by

$$\mathbf{V}_{\alpha\beta, \text{meas}} = \mathbf{V}_{\alpha\beta, \text{actual}} + \Delta \mathbf{V}_{\alpha\beta} . \quad (57)$$

In this case, the PMSM dynamics can be expanded to include the measurement error:

$$\dot{\mathbf{x}} = \mathbf{A}_\omega \mathbf{x} + \mathbf{B}(\mathbf{V}_{\alpha\beta, \text{meas}} - \Delta \mathbf{V}_{\alpha\beta}) , \quad (58)$$

and the reference model becomes

$$\dot{\hat{\mathbf{x}}} = \mathbf{A}_\omega \hat{\mathbf{x}} + \mathbf{B}\mathbf{V}_{\alpha\beta, \text{meas}} + \mathbf{G}\mathbf{C}(\mathbf{x} - \hat{\mathbf{x}}) . \quad (59)$$

Therefore, the error dynamics are

$$\dot{\mathbf{e}} = (\mathbf{A}_\omega - \mathbf{G}\mathbf{C})\mathbf{e} - \mathbf{B}\Delta \mathbf{V}_{\alpha\beta} . \quad (60)$$

From [18] the steady state solution of (60) for balanced voltage scaling errors and unbalanced voltage offset errors is:

$$\begin{bmatrix} e_{3,ss,Vscale} \\ e_{4,ss,Vscale} \end{bmatrix} = \frac{\Delta \mathbf{V}}{\omega_e} \begin{bmatrix} \cos(\theta(t) + \phi) \\ \sin(\theta(t) + \phi) \end{bmatrix} , \quad (61)$$

$$\begin{bmatrix} e_{3,Voff} \\ e_{4,Voff} \end{bmatrix} = \frac{1}{\omega_e \lambda_1 \lambda_2} \begin{bmatrix} \Delta v_\beta (\lambda_1 \lambda_2 - \omega_e^2) - \Delta v_\alpha \omega_e (\lambda_1 + \lambda_2) \\ \Delta v_\alpha (\omega_e^2 - \lambda_1 \lambda_2) - \Delta v_\beta \omega_e (\lambda_1 + \lambda_2) \end{bmatrix} , \quad (62)$$

respectively, where ΔV , Δv_α , and Δv_β are the magnitudes of the balanced voltage scaling error, and the offset error in the fictitious two phase windings.

For a balanced scaling error on the voltage sensor, the solution for the resulting angle estimation error is determined in [18], which gives:

$$\begin{aligned}\hat{\theta} &= \tan^{-1} \left(\frac{\sin(\theta + \delta_{v-scale})}{\cos(\theta + \delta_{v-scale})} \right) = \theta + \delta_{v-scale} \\ \delta_{v-scale} &= \tan^{-1} \left(\frac{\Delta V \sin \phi}{\omega_e \left(\sqrt{\frac{3}{2}} \lambda_m - \frac{\Delta V}{\omega_e} \cos \phi \right)} \right) .\end{aligned}\quad (63)$$

This result clearly shows that the resulting angle estimation error is a constant angle for a balanced sensor scaling inaccuracy. Under these conditions, the circular locus of the estimated states is rotated by the angle $\delta_{v-scale}$ much like the locus shown previously for stator resistance and inductance uncertainties.

In the case that the scaling error is not balanced between the phases, the estimated state locus becomes non-circular, and an angle estimation error of double the fundamental rotational frequency is superimposed upon the constant estimation error angle $\delta_{v-scale}$. The estimated state locus, estimated states, and angle estimation error are each shown in Figure 8 for an unbalanced voltage scaling error.

In the case of voltage offset error, examination of (62) reveals that a constant error that is not a function of the rotor angle is introduced into the estimated state variables. This results in an estimated state locus that is not centered at the origin. Furthermore, if the voltage measurement offsets are not balanced, the locus becomes non-circular, as shown in Figure 9.

The translated locus in Figure 9 generates an angle estimation error at the fundamental frequency, while a non-circular locus creates an additional error term at twice the fundamental frequency. The peak magnitude of the angle estimation error in the case of unbalanced voltage offset is

$$\Delta \hat{\theta}_{p, Voffset} = \frac{\sqrt{e_{3ss, Voff}^2 + e_{4ss, Voff}^2}}{\sqrt{\frac{3}{2}} \lambda_m} .\quad (64)$$

Thus, from (62) and (64) it can be seen that selecting the magnitude of the closed-loop eigenvalue reals to be much greater than the angular velocity helps to reduce the effect of voltage measurement offsets on the rotor position estimation accuracy.

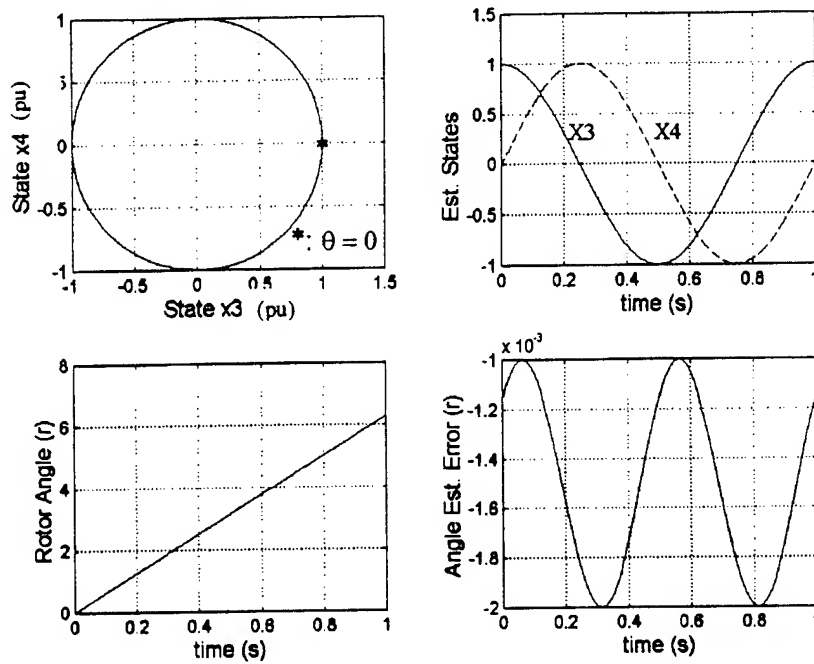


Figure 8. Effect of unbalanced voltage sensor scaling error.

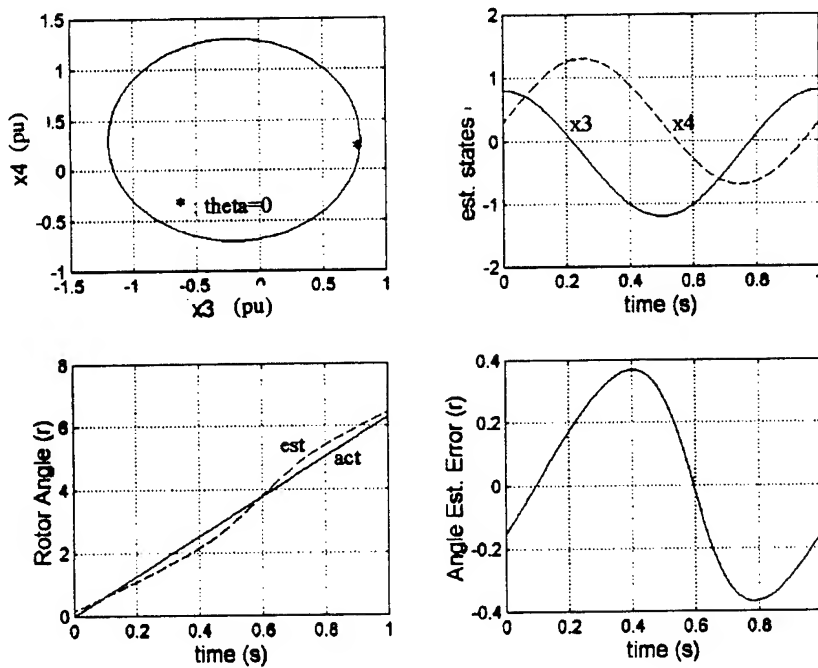


Figure 9. Effect of voltage measurement offset of angle estimation.

2.5.5.2 Current Measurement Errors

In the case of current measurement inaccuracies, the actual and measured signals are related by

$$\mathbf{I}_{\alpha\beta, \text{meas}} = \mathbf{I}_{\alpha\beta, \text{actual}} + \Delta \mathbf{I}_{\alpha\beta} \quad , \quad (65)$$

Where $\mathbf{I}_{\alpha\beta, \text{meas}}$, $\mathbf{I}_{\alpha\beta, \text{actual}}$, and $\Delta \mathbf{I}_{\alpha\beta}$ represent the measured and actual stator currents, and the error associated with the measurement, respectively. With the current measurement relations defined, the output equation (7) is modified to account for the current measurement inaccuracy:

$$\mathbf{y} = \mathbf{C}\mathbf{x} = \mathbf{I}_{\alpha\beta, \text{actual}} = \begin{bmatrix} I_{\alpha, \text{meas}} - \Delta I_{\alpha} \\ I_{\beta, \text{meas}} - \Delta I_{\beta} \end{bmatrix} \quad . \quad (66)$$

The reference model may be expanded to include the current measurement uncertainty:

$$\dot{\hat{\mathbf{x}}} = \mathbf{A}_w \hat{\mathbf{x}} + \mathbf{B}\mathbf{u} + \mathbf{G} \left((\mathbf{I}_{\alpha\beta, \text{actual}} + \Delta \mathbf{I}_{\alpha\beta}) - \hat{\mathbf{i}}_{\alpha\beta} \right) \quad . \quad (67)$$

Thus, the error dynamics are

$$\dot{\mathbf{e}} = (\mathbf{A}_w - \mathbf{G}\mathbf{C})\mathbf{e} - \mathbf{G}\Delta \mathbf{I}_{\alpha\beta} \quad . \quad (68)$$

From Appendix B of [18], the steady state solutions to (68) for current scaling and offset errors are:

$$\begin{bmatrix} e_{3ss, \text{scale}} \\ e_{4ss, \text{scale}} \end{bmatrix} = \Delta \mathbf{i} \begin{bmatrix} L \sin(\theta + \phi) - \frac{R}{\omega_e} \cos(\theta + \phi) \\ -\frac{R}{\omega_e} \sin(\theta + \phi) - L \cos(\theta + \phi) \end{bmatrix} \quad , \quad (69)$$

and

$$\begin{bmatrix} e_{3, \text{off}} \\ e_{4, \text{off}} \end{bmatrix} = \frac{1}{\omega_e \lambda_1 \lambda_2} \begin{bmatrix} -R\Delta I_{\beta} (\lambda_1 \lambda_2 - \omega_e^2) + R\Delta I_{\alpha} \omega_e (\lambda_1 + \lambda_2) \\ -R\Delta I_{\alpha} (\omega_e^2 - \lambda_1 \lambda_2) + R\Delta I_{\beta} \omega_e (\lambda_1 + \lambda_2) \end{bmatrix} \quad . \quad (70)$$

The terms Δi , ΔI_{α} , and ΔI_{β} represent the magnitude of the balanced current scaling error, and current offsets in the α and β axes, respectively.

The effect of current sensor scaling errors on the angle estimation accuracy is computed in Appendix B of [18]. For the balanced current scaling error, the introduced angle estimation error is

$$\begin{aligned}\hat{\theta} &= \tan^{-1} \left(\frac{\sin(\theta + \delta_{I, scale})}{\cos(\theta + \delta_{I, scale})} \right) = \theta + \delta_{I, scale} \\ \delta_{I, scale} &= \tan^{-1} \left(\frac{\Delta i \left(-R \frac{\sin \phi}{\omega_e} + L_s \cos \phi \right)}{\sqrt{\frac{3}{2}} \lambda_m + \frac{R \Delta i}{\omega_e} \cos \phi - \Delta i L_s \sin \phi} \right),\end{aligned}\quad (71)$$

Therefore, a balanced current scaling error introduces a constant angle estimation error of $\delta_{I, scale}$, whose magnitude is dependent on the magnitude of the scaling error. From (71), the angle estimation error is more prone to current scaling errors at low speeds. Similar to the voltage measurement scaling error, any unbalance in the current scaling error vector will generate a double frequency angle estimation error term that is superimposed onto the angle $\delta_{I, scale}$.

From (71), the effect of current offset error is a constant term added to the estimated states. Thus, current offset is identical in nature to the voltage offset error described in the previous section with the exception that the amplitude of the angle estimation error in the current offset case is

$$\Delta \hat{\theta}_{p, offset} = \frac{\sqrt{e_{3ss,loff}^2 + e_{4ss,loff}^2}}{\sqrt{\frac{3}{2}} \lambda_m}. \quad (72)$$

2.6 Eigenvalue Selection Strategy

The observer poles should be selected according to the system requirements, which are typically rapid response and stable estimation. As the real parts of the eigenvalues become larger negative values, the estimation error converges rapidly. Choosing the eigenvalues too aggressively, however, results in the amplification of system noise and reduced or even unstable performance.

A general algorithm for observer pole placement was presented in (21), where it is suggested that the observer poles be placed based on the rotor velocity. Furthermore, the results of the angle estimation error study indicate that choosing observer poles much faster than the angular velocity of the PMSM reduces the effects of angular velocity estimation uncertainty as well as voltage and current measurement errors. Velocity

estimation using the time derivative of the estimated rotor angle is also improved by choosing fast observer eigenvalues with respect to angular velocity, as shown in [18].

In the sensorless drive technology demonstrator system, the eigenvalues of the position observer were scheduled according to the angular velocity as indicated in (21). Through experimentation, it was found that observer poles at least 4 times faster than the angular velocity produced excellent results. Thus in (21), the pole placement was performed with $k_{\lambda-real} \geq 4$ and $k_{\lambda-imag} = 1/2 k_{\lambda-real}$. The real part is chosen for stability purposes while the imaginary part was found through experimentation to produce desirable damping characteristics.

3 SENSORLESS DRIVE IMPLEMENTATION

In this chapter, the rotor position estimation algorithm outlined in Chapter 2 is implemented on a digital signal processor (DSP). The processing hardware, associated power electronics, and sensors used to realize the sensorless drive technology demonstrator are presented and implementation details are discussed.

3.1 Control Implementation

Electric drives are used to control the torque and speed of a motor in a closed loop system. A resolver or encoder attached to the shaft of the motor is normally used to provide the feedback required to carry out the torque and velocity control loops. In the sensorless drive technology demonstrator, however, the rotor position and velocity are supplied by the rotor angle and velocity estimator, respectively.

The arrangement of the sensorless controller is shown in Figure 10, where cascaded torque and speed loops are shown. The actual drive is shown in Figure 11. The outer velocity loop generates the torque reference required to drive the speed of the PMSM shaft toward its commanded value. From the torque command and knowledge of the rotor angle, balanced, three phase current commands that are required to produce the commanded torque are generated. The PWM current controller then applies the required voltage, via the inverter, to the PMSM terminals in order to enforce the current references.

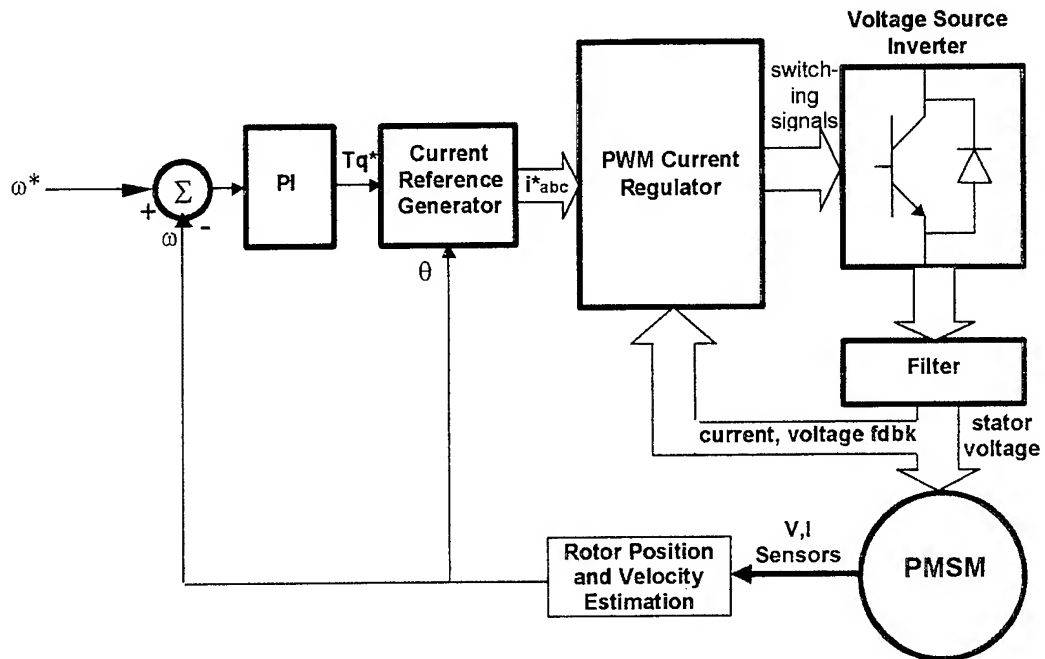


Figure 10. Block diagram of sensorless PMSM drive system.

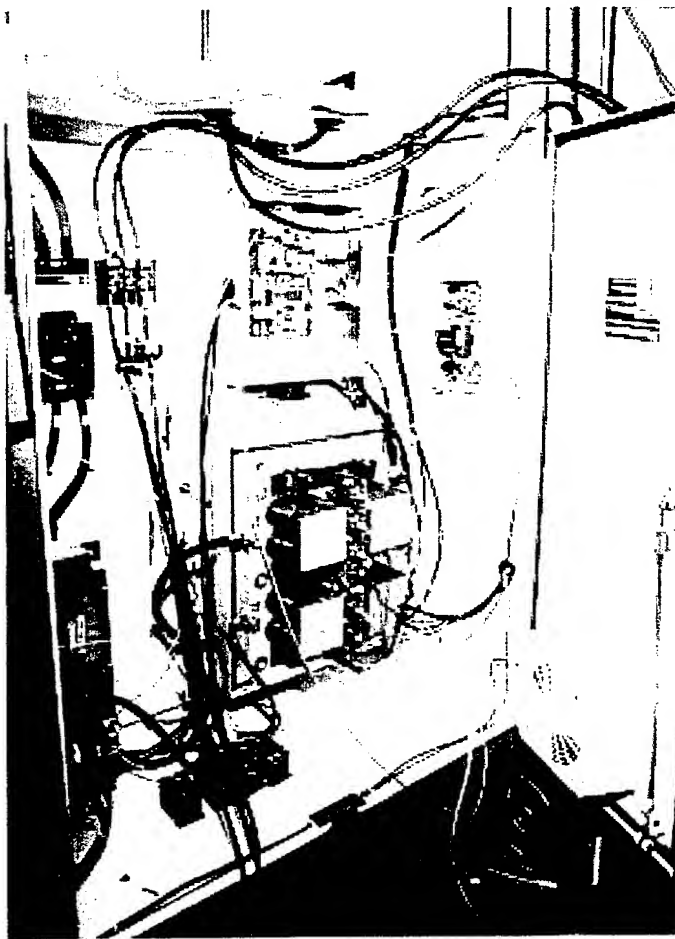


Figure 11. Actual sensorless PMSM drive.

3.1.1 Current Controller

The innermost torque control loop is clearly the most important loop in the cascaded control structure shown in Figure 10. In order to obtain optimum performance of the entire system, including the outer velocity loop, requires that the developed instantaneous torque is equal to the commanded torque. In the sensorless drive system, the torque controller is implemented through a current regulator, since the developed torque is directly proportional to the quadrature axis current in the PMSM [20]. The current regulator consists of a voltage source PWM inverter, where the sinusoidal PWM method [21] is used.

In the current regulator of the sensorless electric drive, a PI controller in the rotating reference frame has been adopted [22, 23]. Current control is greatly simplified in the rotating reference frame, making a three-phase machine equivalent to analyzing a DC motor. The rotating reference frame current controller operated on DC quantities, and can in theory regulate the currents with zero steady-state error.

The current controller implemented in the sensorless drive is based on the technique presented in [22]. The machine model in the synchronous reference frame is given as

$$\begin{bmatrix} v_d \\ v_q \end{bmatrix} = \begin{bmatrix} L_d & 0 \\ 0 & L_q \end{bmatrix} \begin{bmatrix} \dot{i}_d \\ \dot{i}_q \end{bmatrix} + \begin{bmatrix} R & -\omega_e L_q \\ \omega_e L_d & R \end{bmatrix} \begin{bmatrix} i_d \\ i_q \end{bmatrix} + \sqrt{\frac{3}{2}} \omega_e \lambda_m \begin{bmatrix} 0 \\ 1 \end{bmatrix}. \quad (73)$$

In (73), $v_{d,q}$ and $i_{d,q}$ represent the motor inputs and outputs, respectively in the direct and quadrature axes. In the synchronous reference frame, the induced emf $\sqrt{3/2} \lambda_m \omega_e$ in the quadrature axis current is a slowly varying disturbance proportional to angular velocity. In addition, (73) shows a cross coupling of the direct and quadrature axis currents into the quadrature and direct axis voltage expressions, respectively. If the disturbance and cross coupling terms are decoupled from (73), the dependence on angular velocity disappears and the stator voltage equation becomes that of an RL (resistance and inductance) load, enabling simple, fast, and accurate current regulation.

Through feedback linearization, a decoupled and linear system can be obtained by choosing

$$\begin{bmatrix} v_d \\ v_q \end{bmatrix} = \begin{bmatrix} v'_d \\ v'_q \end{bmatrix} + \begin{bmatrix} v_d^\omega \\ v_q^\omega \end{bmatrix}, \quad (74)$$

where v'_d and v'_q are the modified output voltages of the current regulator, v_d and v_q are the actual voltages applied to the PMSM, and v_d^ω and v_q^ω are the decoupling terms :

$$\begin{bmatrix} v_d^o \\ v_q^o \end{bmatrix} = \begin{bmatrix} 0 & -\hat{\omega}_e L_q \\ \hat{\omega}_e L_d & 0 \end{bmatrix} \begin{bmatrix} i_d \\ i_q \end{bmatrix} + \sqrt{\frac{3}{2}} \hat{\omega}_e \lambda_m \begin{bmatrix} 0 \\ 1 \end{bmatrix}. \quad (75)$$

In (75), the decoupling vector \mathbf{v}_{dq}^o is used to overcome the rotor velocity-dependent cross coupling and motor back emf terms. Note that in a sensorless drive, the calculation of the cross-coupling term must use the estimated rotor velocity $\hat{\omega}_e$. With the cross coupling vector defined, the system may be described by

$$\begin{bmatrix} \dot{i}_d \\ \dot{i}_q \end{bmatrix} = \begin{bmatrix} 1/L_d & 0 \\ 0 & 1/L_q \end{bmatrix} \left\{ \begin{bmatrix} v_d' \\ v_q' \end{bmatrix} - R \begin{bmatrix} i_d \\ i_q \end{bmatrix} \right\}, \quad (76)$$

to which linear control design techniques can be applied. In the prototype sensorless drive, a PI controller is utilized such that

$$v_d' = K_p + \frac{K_i}{s} (i_d^* - i_d) \quad ; \quad v_q' = K_p + \frac{K_i}{s} (i_q^* - i_q). \quad (77)$$

The proportional and integral gains, K_p and K_i , are selected to be equal in the d and q axis current controllers, and are determined experimentally to give a closed loop current controller of sufficient bandwidth - approximately 1 kHz in the demonstrator system.

A functional block diagram of the current control used on the prototype sensorless drive is shown in Figure 12. In a velocity control application, an outer velocity controller generates the current or torque command Tq^* , which is translated to d - q current commands by the reference current generator. The direct axis current reference i_d^* is normally maintained at zero, since does not produce torque in a non-salient PMSM. That is, the quadrature axis current command i_q^* represents the primary torque-producing component.

In Figure 12, the feedback currents are transferred into the rotating reference frame through Park and Clarke transforms and the rotor angle, which is generated by the rotor position estimator. Comparison of the current reference to the feedback yields the current error, which is operated on by the PI controller to generate the voltage references in the rotating reference frame. Finally, the voltage reference is transformed to voltage commands in the stationary frame, which are operated on by the PWM controller to generate the inverter switching control signals. Only two current values are measured by the DSP since the third phase current is not an independent variable for a Y-connected PMSM.

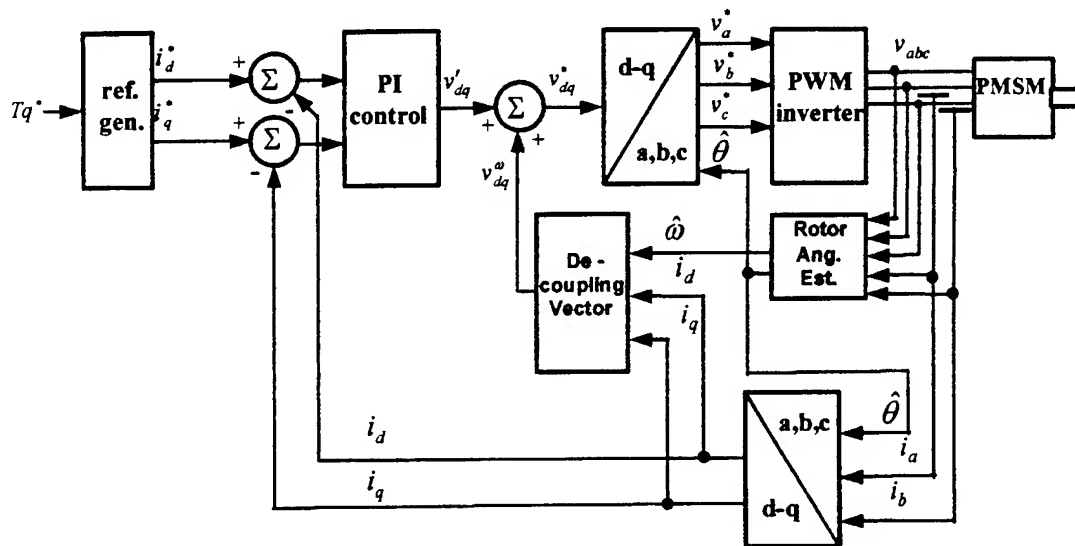


Figure 12. PMSM current control block diagram.

In order to demonstrate the effectiveness of the current control scheme, some experimental results are now presented. In the experiments, the proposed current controller is implemented on a digital signal processor in a closed loop system with a DC link voltage of 650 volts.

In Figure 13, the current control performance in steady state is shown for an operating speed of 300 RPM, and load torque of approximately 200 foot-pounds. Figure 14 demonstrates the transient performance during a step change in the quadrature-axis current command, which occurs at approximately 200 milliseconds when a speed reversal is requested. This results show that the current controller exhibits very fast control response without overshoot.

For the startup transient shown in Figure 15, the quadrature axis current is required to increase with the speed due to the viscous loading on the system. In the figure, it can be seen that any errors in the estimated rotor angle can produce unexpected results, since accurate rotor angle feedback is required to correctly control the torque via the quadrature axis current.

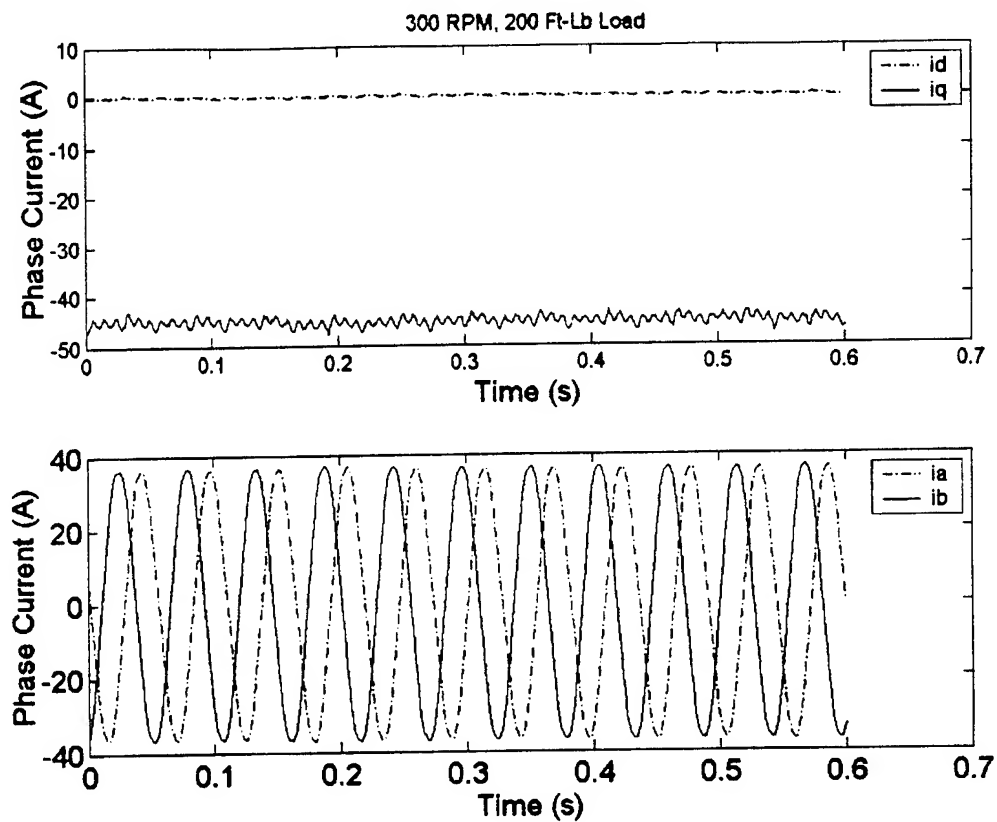


Figure 13. Current controller performance during steady state.

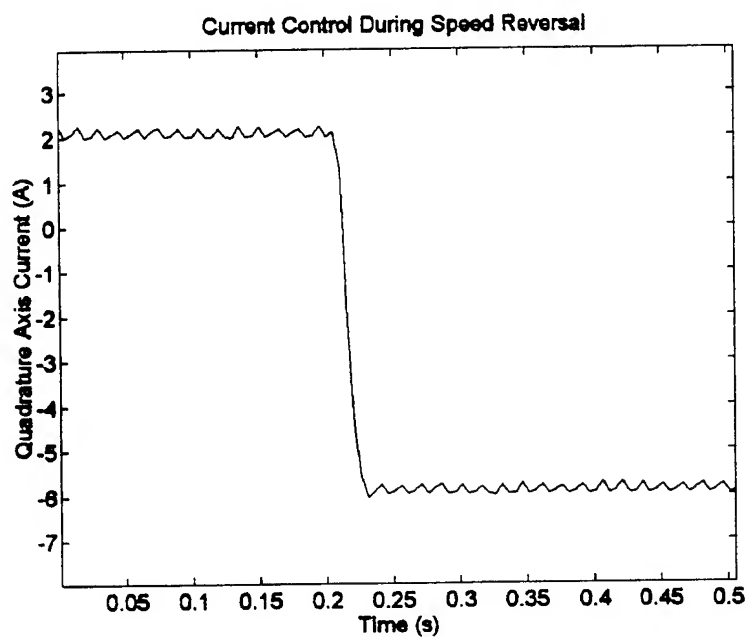


Figure 14. Current controller performance during speed reversal transient.

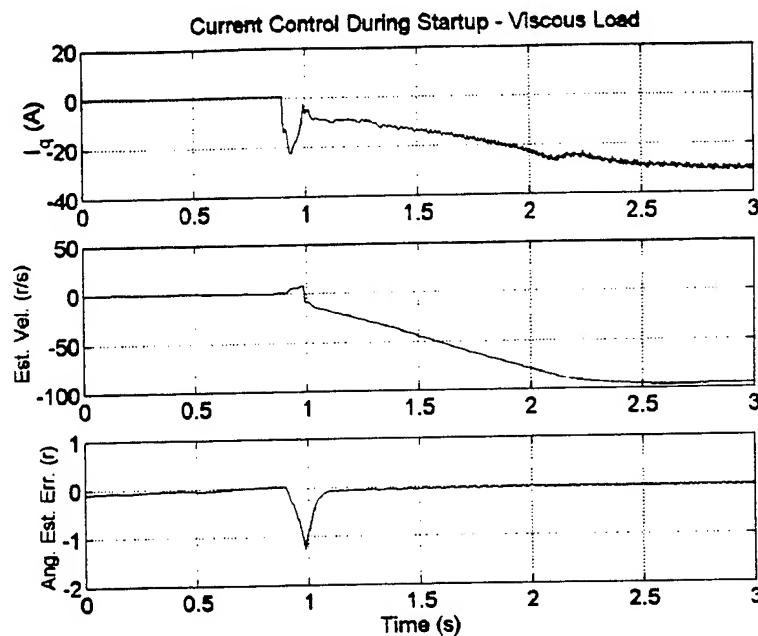


Figure 15. Current control during startup transient.

3.1.2 Velocity Controller

In order to implement velocity control, a proportional-integral (PI) speed control has been implemented. Since this is a sensorless drive, the velocity controller utilizes the estimated angular velocity (described in Chapter 2) as the feedback. The PI controller operates on the speed error to generate the torque command, as depicted in Figure 10.

Steady state speed control performance in the sensorless mode is demonstrated in the experiment illustrated in Figure 16, where the actual velocity is obtained from an encoder signal temporarily attached to the shaft of the motor under test. In this experiment, the commanded velocity is -300 RPM, the mean value of the estimated velocity is -300.1016 RPM, and the mean value of the actual rpm is -300.0487 RPM. The results shown in Figure 16 reveal that any error associated with the estimated angular velocity generates a corresponding ripple in the actual speed. A 2nd order filter with a cutoff frequency of 50 r/s conditions the estimated angular velocity. While a lower cutoff frequency would reduce the amplitude of the ripple on the estimated velocity, it would also have an adverse effect on transient performance.

Figure 17 demonstrates that during a speed reversal transient, filtering of the estimated angular velocity results in a delay between the actual and estimated angular velocity. This delay is seen to generate difficulties in angle estimation – especially when the estimated angular velocity is opposite in polarity to the actual estimated angular velocity. In general, if the estimated and actual angular velocity are of opposite sign only when observer feedback is disabled (i.e. when operating below the low speed threshold), the estimated angle error will recover from the error in angular velocity. This is shown in the figure where the angle estimation error converges toward zero when the angular velocity

exceeds the low speed threshold of 19 RPM (at approximately 1 second). However, if the estimated and actual angular velocities are of opposite polarity while operating above the low-speed threshold level, the observer becomes unstable. This is clearly an undesirable situation, and illustrates the considerations in selecting the cutoff frequency of the estimated angular velocity filter. The selection of this cutoff frequency represents a tradeoff between steady-state and transient velocity control performance.

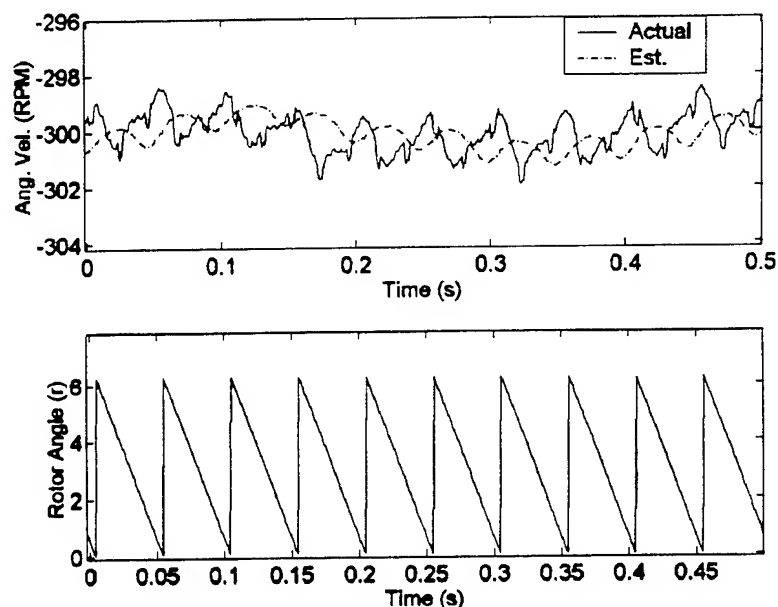


Figure 16. Sensorless velocity control – steady state 300 rpm.

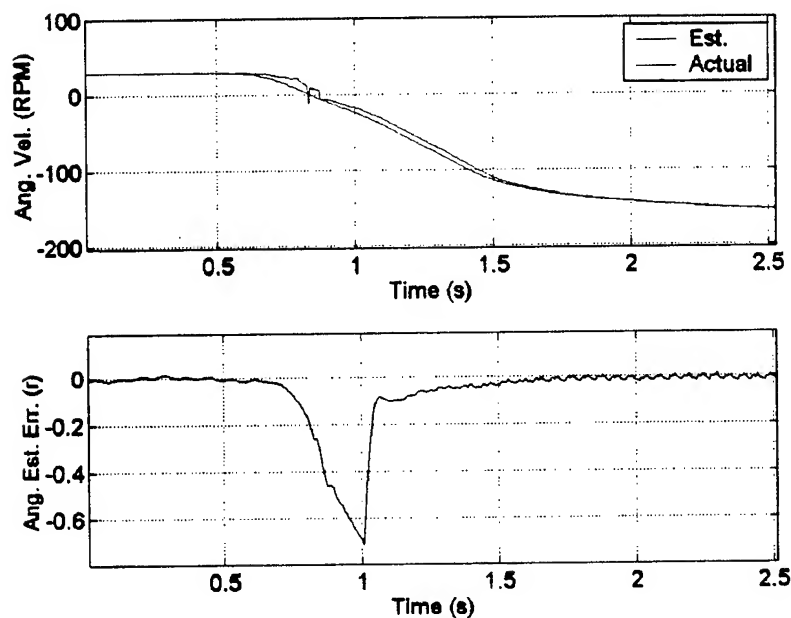


Figure 17. Sensorless velocity control – speed reversal.

3.2 Hardware and Algorithm Implementation

In this section, the implementation of the rotor position estimation strategy in a closed-loop drive system is presented. Although many sensorless control algorithms have been proposed in literature, very few have actually demonstrated the drive performance in a closed-loop system. Therefore, some issues and strategies related to the implementation are described.

3.2.1 Computing Hardware

The architecture for the computing hardware of the prototype sensorless electric drive consists of a floating point digital signal processor (DSP) and a fixed point motor control DSP. A block diagram of the arrangement is shown in Figure 18, and photographs of the controller board are included in Figure 19. In the demonstrator sensorless drive system, a personal computer acts as the user interface, providing a graphical user interface for operating the drive, displaying the drive performance status, and storing relevant operational data. The developed computing hardware has been designed to perform sensorless control for a specific Integrated Motor/Propulsor drive application [17]. Both DSPs are bootable from a programmable, erasable memory device (EPROM).

The floating point DSP (Analog Devices model EZ-Kit Lite) performs the rotor position and velocity estimation at 100 μ s and 2 ms intervals, respectively. The fixed point motor control DSP (Analog Devices ADMC401) is used to implement the current control scheme previously described, sample the stator voltages and currents, and provide the PWM signals to the inverter. The PWM frequency for the sensorless drive is 15 kHz.

The two DSPs communicate directly through the dual-port memory bank resident on the floating point DSP. This dual-port memory, which is divided into read-only and write-only blocks to avoid simultaneous writes to the same location by the two processors, allows the two processors to share all required data with little overhead. The floating point DSP provides the rotor angle estimate and current commands to the motor control DSP, while the motor control DSP supplies the measured currents and voltages to the floating point DSP.

3.3 Software Development

In the DSP implementation, the digital controller is constructed from the continuous-time observer equations (6), (7), (10) and (11) using the forward Euler integration method. The development of the software was carried out using the Analog Devices programming tools for the Sharc DSP, and the motion control debugger for the fixed point motor control DSP. The floating and fixed point devices were programmed in C and assembly language, respectively. The PMSM angular velocity and angle estimation algorithms are scheduled to execute periodically in the sequence indicated by Figure 20, which shows program flow and execution times.

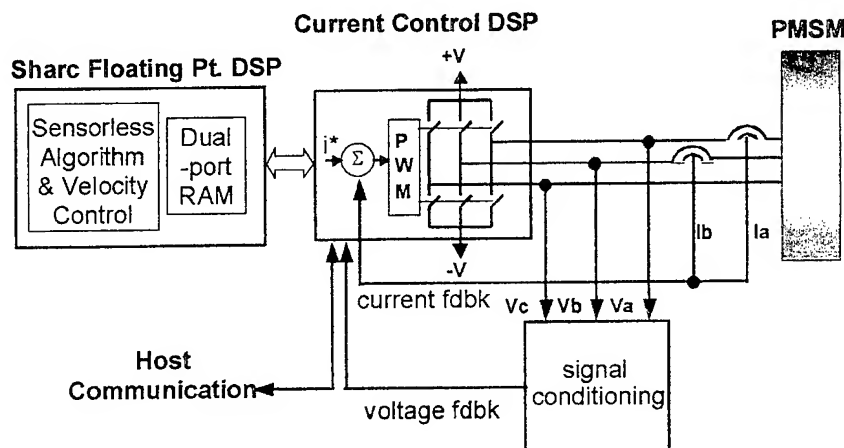


Figure 18. Block diagram of prototype sensorless drive hardware.

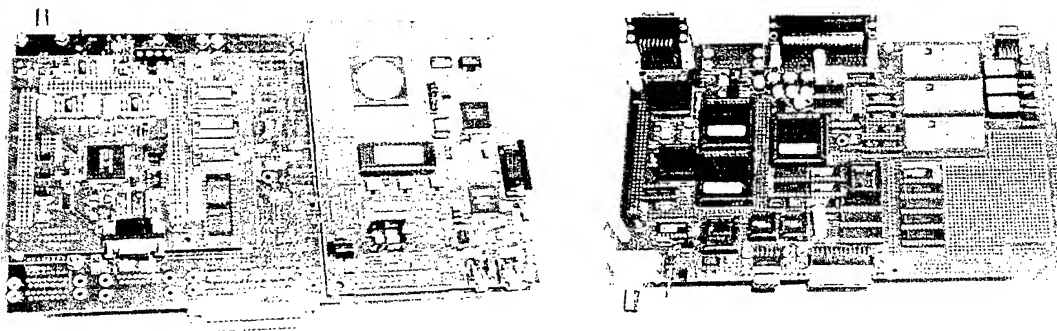


Figure 19. Dual-DSP processing hardware- top view (left), bottom view (right).

For each sampling interval of the floating point DSP ($100 \mu\text{s}$), the observer requires input voltages and output currents. These quantities are simultaneously sampled at the center point of each PWM cycle [1] by the motor control DSP by the analog-to-digital converter of the motor control DSP. The acquired sensor data is then written to the dual port memory, making it available to the observer. The floating point DSP operates on the acquired data to update the estimated state variables and rotor angle. The estimated angle is transmitted back to the motor control DSP along with the most recent velocity estimate and torque command. These quantities are required by the motor control DSP to execute the torque control cycle. The floating point DSP is programmed to estimate the angular velocity every n th cycle time, where $n=20$ for the demonstrator drive system. The observer gain matrix G is updated with each velocity estimation cycle.

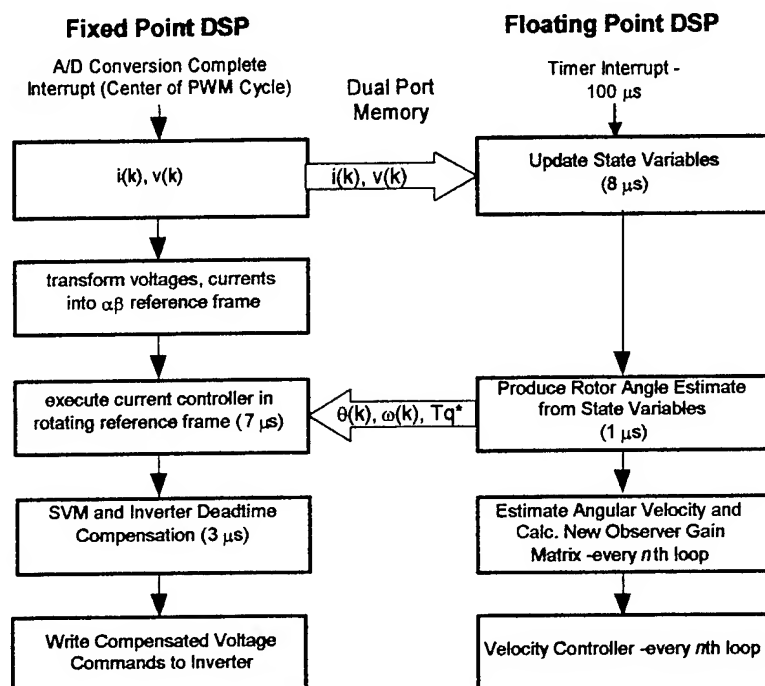


Figure 20. Program flow diagram for sensorless drive implementation.

3.3.1 Sensors

The use of the PWM inverter is nearly universal in PMSM drives, making accurate voltage and current measurements problematic due to the switching nature of the applied voltage. Due to the electrically noisy environment surrounding a typical PWM inverter, the acquisition of high quality measurements required by the rotor position observer is not a trivial undertaking. The following sections describe the sensing elements and technique used to acquire the PMSM phase voltages and currents.

3.3.1.1 Voltage Measurements

The approach to acquiring the PMSM phase voltage in the demonstrator sensorless drive is the direct measurement approach [1]. Implementation of the direct measurement technique requires both electrical isolation and low-pass filtering in order to isolate power and signal grounds, and to remove high frequency switching components of the phase voltage, respectively. A block diagram of the configuration used to directly measure the phase voltage is shown in Figure 21.

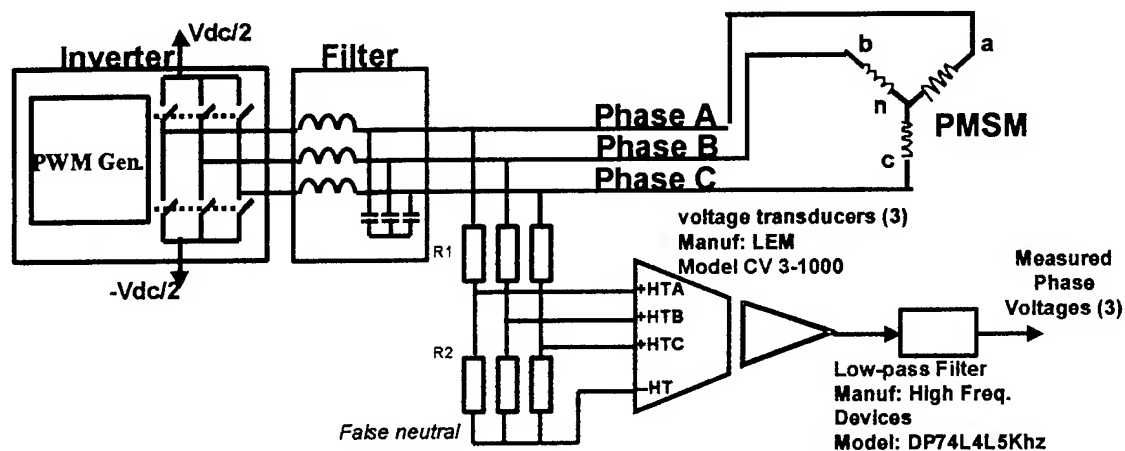


Figure 21. Block diagram of direct phase voltage measurement.

In Figure 21, a resistive divider is used to scale the motor terminal voltage and to form a *false neutral* node, which under normal conditions is at the same potential as the buried PMSM neutral. The voltage transducer (LEM Model CV 3-1000) provides an isolated signal, which is low-pass filtered before being sampled by the motor control DSP analog-to-digital converter. The voltages are sampled synchronously to the PWM frequency at the PWM center point, as described in [1]. This sampling strategy reduces the effect of PWM ripple on the sampled data. The voltage transducer has a bandwidth of 500 kHz so that it does not distort the unfiltered voltage signal.

The low-pass filter is a 4th order Bessel filter with a cutoff frequency of 5 kHz (Frequency Devices model DP74L4L5kHz). Despite the use of the line filter between the inverter and PMSM, a filter is still required to further remove the high frequency switching signal from the voltage measurements. The drawback, however, is that the use of the 4th order filter introduces in a time delay of approximately 68 μ seconds in the voltage signal. This delay contributes a predictable angle estimation error at higher frequencies. This phenomenon will be shown and discussed in the experimental results of Chapter 4.

It should be noted that the indirect voltage measurement technique discussed in [1], which uses a combination of the DC link voltage and the commanded PWM duty cycles is problematic in large drive systems where an output filter is used, since the output filter parameters must be accurately known to determine the voltages present at the motor terminal.

3.3.1.2 Current Measurements

In any servo application, current feedback is required to close the torque control loop. That is, current measurements are required in either sensor-based or sensorless PMSM drives. Like the voltage signals, the current waveform can contain higher frequency components due to the PWM driven inverter. Sampling the current synchronously with

the PWM waveform relieves this situation by reducing the effect of PWM ripple on the sampled data. In doing so each of the sideband harmonics are symmetric about the PWM switching frequency harmonic. By sampling at the PWM switching frequency, all of the sideband harmonics sum to DC. Furthermore, by sampling at the PWM center point, the sideband harmonics sum to zero.

The demonstrator sensorless PMSM drive uses 200 ampere current transducers (LEM Model LA 205-S). These transducers have a frequency bandwidth of 100 kHz and are very linear through the operating range of the device. Only two of these sensors are required in the demonstrator drive, since the PMSM is connected in the 'Y' configuration and the third phase current is derived from the two measured values. Figure 22 shows the current sensors as installed in the sensorless drive system cabinet.

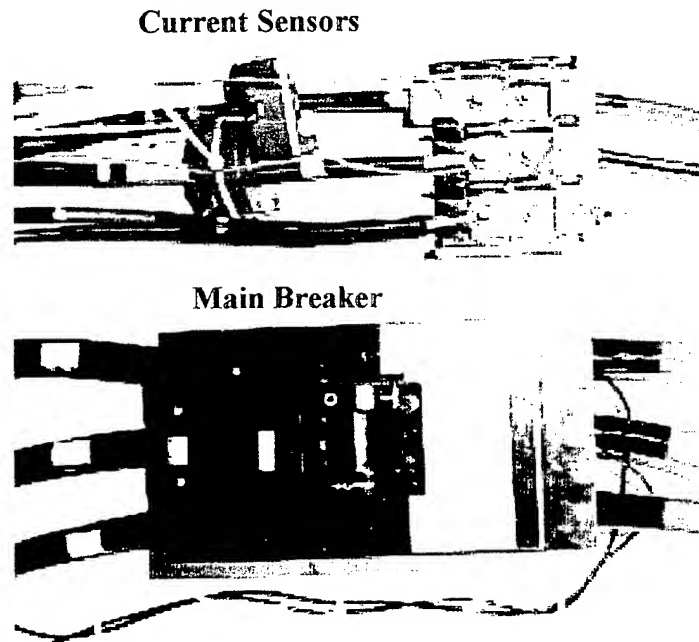


Figure 22. Current sensors and main breaker.

3.3.2 Power Output Stage

The power output stage of the sensorless electric drive system serves to apply commanded voltages to the PMSM terminals. In PMSM drive applications, the most popular power stage consists of a voltage source PWM-driven inverter, which is a DC to AC converter built with IGBTs and configured to deliver bipolar current waveforms to the motor.

In the demonstrator sensorless drive, a commercially available power stage is used (Model IPM1206, Trace Technologies, Livermore, CA). This inverter, which is shown in Figure 23, is capable of operating at DC bus voltages of up to 750 volts, and (with proper cooling) is capable of delivering 150 kW at PWM switching frequencies of up to 15 kHz. The DC link capacitor bank is included in this commercially available power stage.

The motor control DSP provides the PWM switching signals to each of the six IGBT gate drives of the power output stage through a fiber-optic interface (Agilent Technologies Versalink modules). In return, the power stage provides fault enunciation for each IGBT through the same fiber-optic interface. The fiber-optic interface is advantageous due to its immunity to electrical noise and inherent electrical isolation of power electronics and signal-level systems.

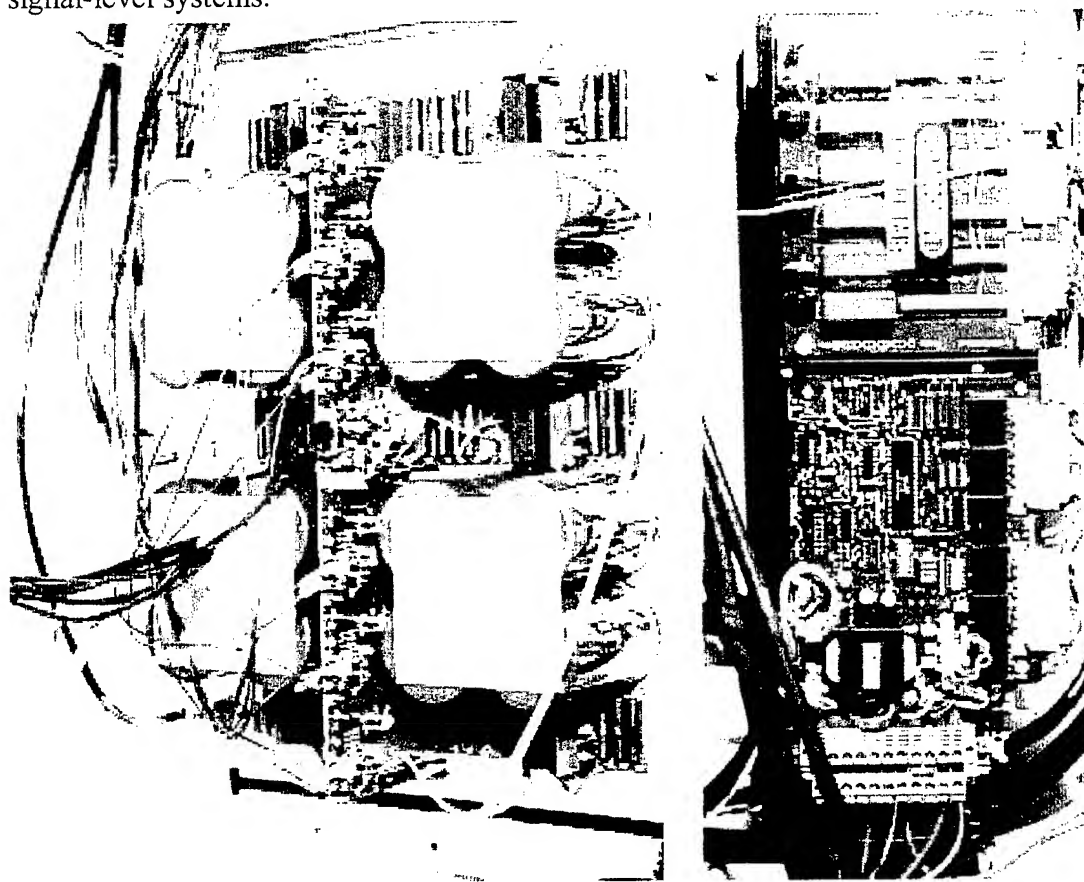


Figure 23. Inverter (left) and AC/DC converter (right) used in sensorless electric drive.

3.3.3 Output Filter

The fast voltage risetime delivered by modern inverter assemblies (<1000 volts/ μ s) has many implications, including an increase in common-mode currents, and damaging overvoltage conditions at the motor terminals when the distance between the motor and the inverter is long. The overvoltage can cause early breakdown of the winding insulation in the motor. Common mode currents may result in increased EMI and increased bearing wear due to the introduction of shaft currents.

To mitigate the undesirable effects of the steep voltage waveforms present in high power drive assemblies, a filter is often employed to limit the risetime of the applied voltage. The output filter used in the sensorless electric drive is comprised of a single stage LC

filter, as shown in Figure 24. The LC filter as shown forms a low pass filter with a characteristic 2nd order 40 db/decade attenuation from the cutoff frequency of

$$\frac{1}{2\pi\sqrt{LC}} \quad (78)$$

The LC filter used (MTE Corporation model RL10013C) is a 75 HP unit that combines the characteristics of line reactors, which are known to limit common mode currents, with the capacitor network to generate a near-sinusoidal output voltage waveform, as shown in Figure 25. The use of such filters is seen to significantly reduce the dv/dt of the output voltage and thus helps to extend motor life by reducing the motor peak voltage.

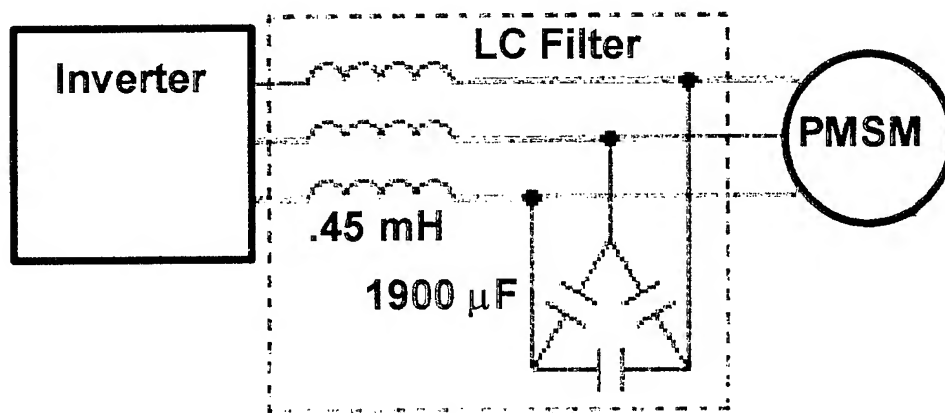


Figure 24. Block diagram of LC filter.

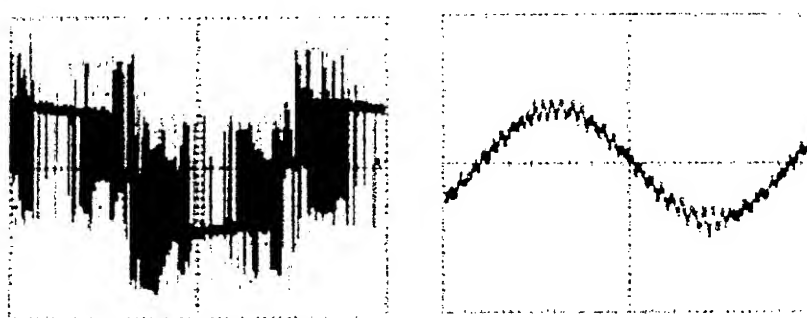


Figure 25 Line voltage without LC filter (left) and with LC filter (right).

3.4 PMSM Motor

The experimental motor used in the sensorless electric drive demonstrator is a 70 HP PMSM manufactured by Electrodynamics Corp division of Electric Boat, Avanel NJ.

The machine was designed for dual-use, and therefore contains separate phase winding connections, as depicted in Figure 26. In the low speed configuration, the individual windings in each of the three phases are connected in series, while for high speed applications, they are connected in parallel. The parameters of the machine are shown in Tables I and II for the low and high speed configurations, respectively.

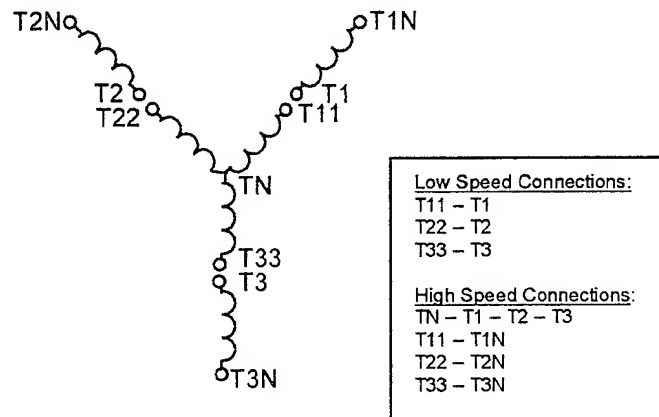


Figure 26. Diagram of PMSM winding configuration.

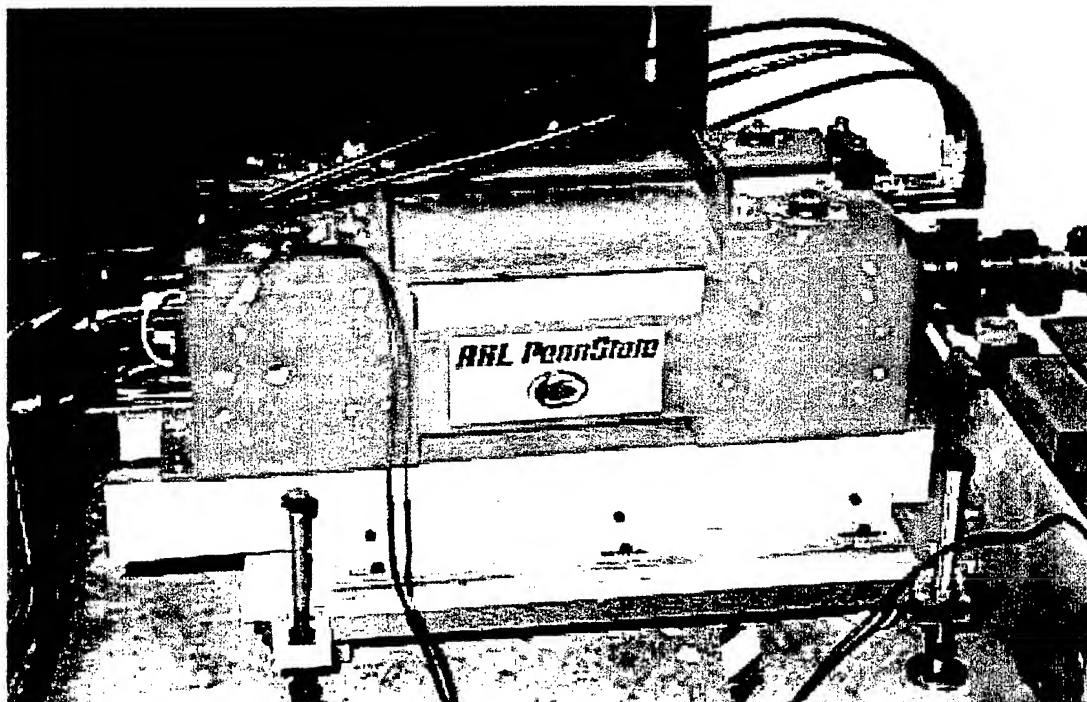


Figure 27. 70 HP PMSM used in sensorless electric drive studies.

Table I. Electrodynamics Corp. motor parameters (low-speed winding configuration).

Parameter	Value
Inductance L_{av}	1.7 mH
Resistance R	.28 Ω
PM Flux Linkage λ_m	1.376 v-s
Rated Power	70 HP
Poles	8

Table II. Electrodynamics Corp. motor parameters (high-speed winding configuration).

Parameter	Value
Inductance L_{av}	.425 mH
Resistance R	.07 Ω
PM Flux Linkage λ_m	0.688 v-s
Rated Power	70 HP
Poles	8

4 SENSORLESS PMSM EXPERIMENTAL RESULTS

In this chapter, the rotor position estimation strategy is operated in a closed-loop drive system, where the drive is implemented as discussed in Chapter 3. To evaluate the performance of the sensorless drive, a set of experiments were performed where the computing hardware executes the complete PMSM control algorithm in real time. Experimental results depicting the rotor position estimation accuracy across the operating range of the PMSM are presented in this chapter for both transient, steady-state, and varying load torque conditions.

4.1 Experimental System

The test setup used in the experiments is shown in Figure 11 (drive electronics) and Figure 28 (motor/load). The mechanical arrangement consists of a PMSM whose shaft is coupled to a pump, which is used to provide load torque. A quadrature shaft encoder (14,400 counts per mechanical revolution) was attached directly to the motor shaft. The encoder was not employed by the drive system, but was used to measure the accuracy of the estimated rotor angle. The drive electronics shown in Figure 11 and the motor shown in Figure 28 are physically separated by approximately 75 feet of cable.

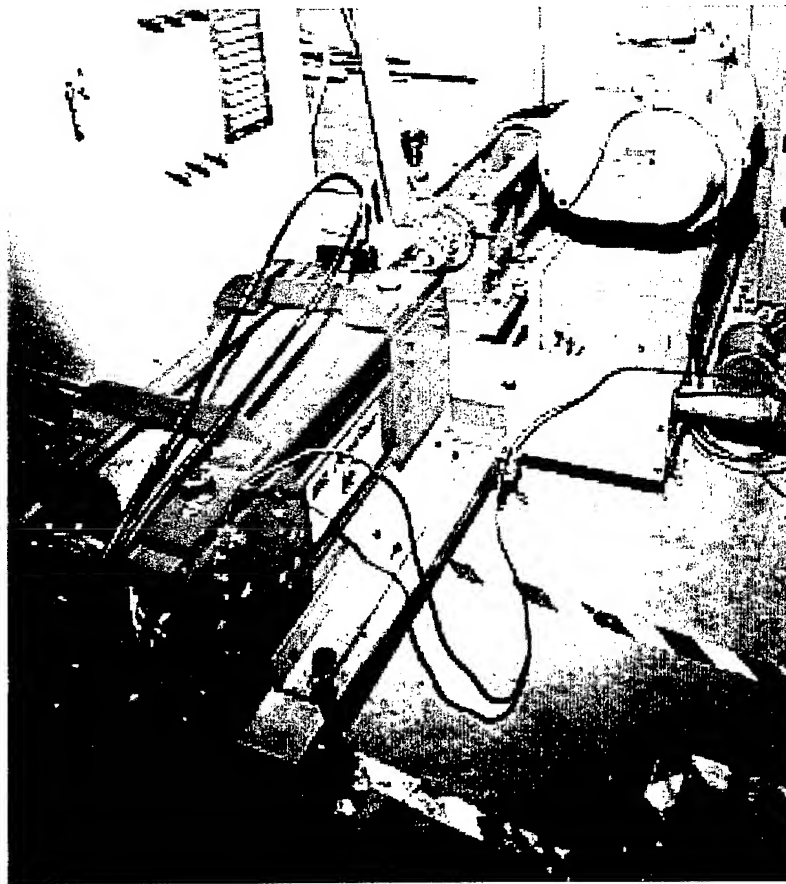


Figure 28. Motor (foreground) and load (background) used in sensorless drive studies.

4.2 Experimental Results

In this section, experiments on the sensorless drive are carried out. All of the experiments are executed using the developed sensorless drive hardware, which controls the PMSM in real-time using the estimated rotor angle and speed. The experiments are intended to demonstrate the effectiveness of the proposed sensorless technique over a wide variety of operating conditions.

4.2.1 Steady State Rotor Position Estimation Accuracy

To determine the angle estimation accuracy, a set of experiments was performed on the drive system across the speed range of the PMSM. The results are shown in Figure 29 and Figure 30, where the rotor position estimation error is shown for the low speed and high speed winding configurations, respectively. For these tests, the PMSM was essentially unloaded. It will be demonstrated in a later section that the angle estimation error is largely independent of load torque.

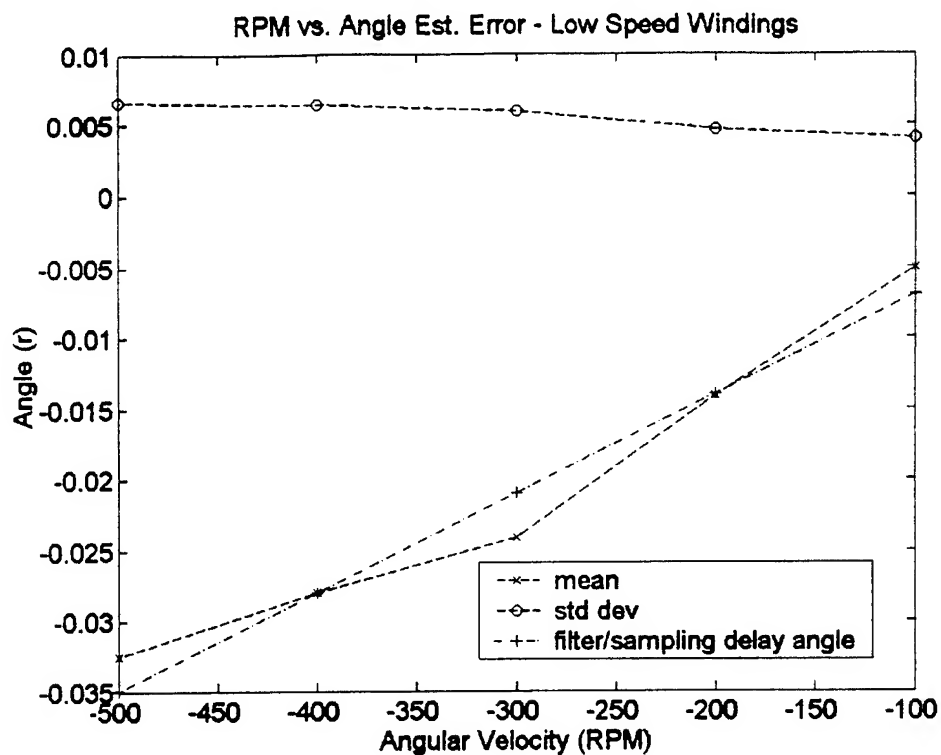


Figure 29. Angle estimation accuracy versus speed for low speed winding configuration.

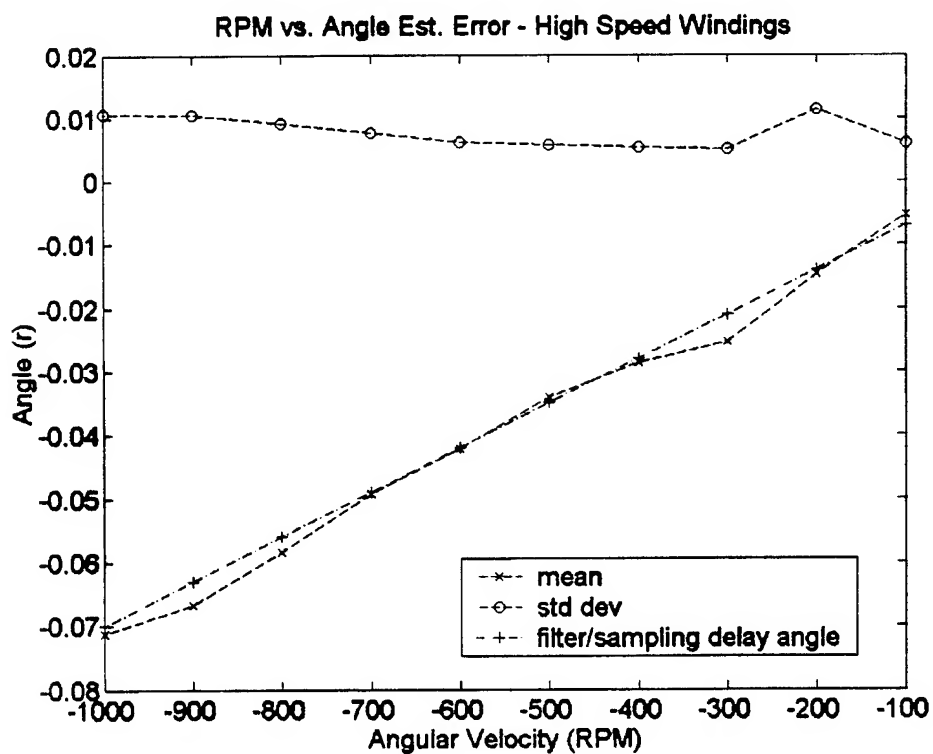


Figure 30. Angle estimation accuracy versus speed for high speed winding configuration.

Although the performance of the rotor position estimator is excellent in Figure 29 and Figure 30, it is clear that the estimation error increases with rotor speed (frequency). This degradation in rotor position estimation performance as speed increases is due to the delay introduced by the low-pass filtering of the phase voltages and the sampling delays introduced by the discrete-time implementation of the algorithm. The filter and sampling delays are $67 \mu\text{s}$ and $100 \mu\text{s}$, respectively. Thus, the net effect is a linear phase shift of the measured phase voltages that is linearly dependent on the operating frequency. The phase shift produces a corresponding frequency-dependent angle estimation error given by

$$\text{phase shift } (r) = 167 \mu\text{s} * \text{Shaft Speed (in } r/s) . \quad (79)$$

For convenience, this expected angle estimation error due to the filtering and sampling delays given in (79) is included in Figure 29 and Figure 30. Clearly, the angle estimation error follows the expected error due to the delays. It should be noted that this speed-dependent estimation error could be easily removed by compensating for the filter/sampling delays, since the error versus speed characteristic is well known from (79).

4.2.1.1 Low Speed Operation

In the sensorless drive, rotor position estimation at and around zero speed present is problematic. In the demonstrator system, this is managed by setting the observer gain matrix G to zero for angular velocities below an experimentally determined low-speed threshold, which essentially disables the observer. Under these operating conditions, the internal PMSM model runs without correctional feedback. The low-speed threshold is 7.5 r/s , or approximately 19 RPM for the 8 pole PMSM used in the studies.

Figure 31 and Figure 32 show the operation of the sensorless drive at extremely low speeds. Figure 31 demonstrates operation at a speed slightly above the low-speed threshold of 19 RPM. In this experiment, the motor runs quite reliably. However, occasional polarity reversals in the estimated velocity occur at such low speeds that tend to generate corresponding deviations in the estimated rotor angle. In situations such as Figure 31, where polarity reversals are rather infrequent and of short duration, the estimated rotor angle error diverges during the estimated velocity polarity reversals, but is quickly adjusted when the angular velocity estimate is corrected.

In Figure 32, the system is operating at 50 RPM, which is more than twice the low-speed threshold. At this speed, the estimated velocity polarity reversals do not occur, and the angle estimation error is much more stable. From a comparison of Figure 31 and Figure 32, it is apparent that the estimation of angular velocity is more problematic at lower speeds. This is due to the difficulty in determining the direction of rotation of the voltage vector described in (15) and (16) when noise is present on the low-amplitude terminal voltage signals.

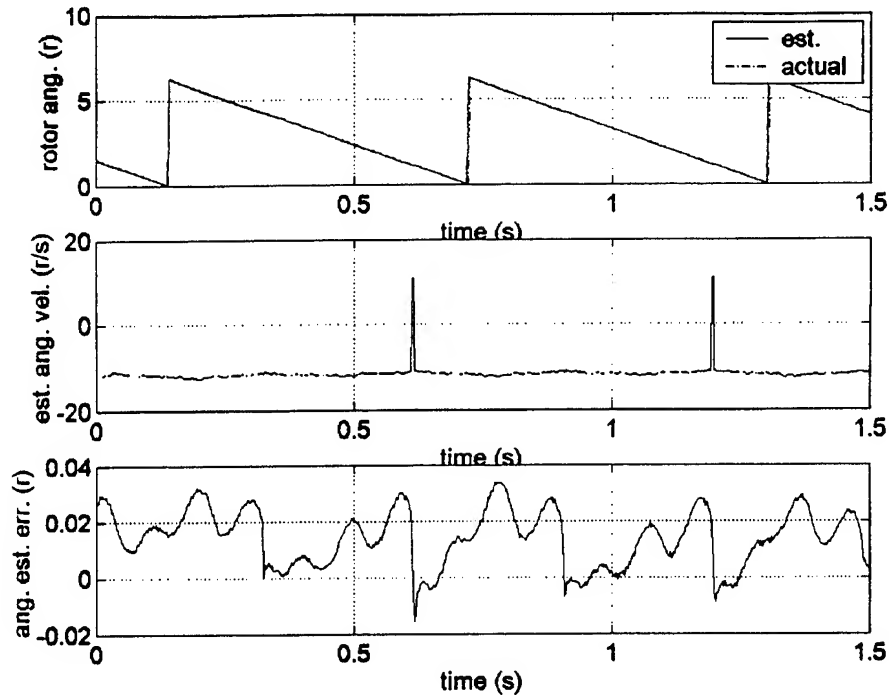


Figure 31. Estimation accuracy at 30 RPM, 10 ft-lb – low speed winding configuration.

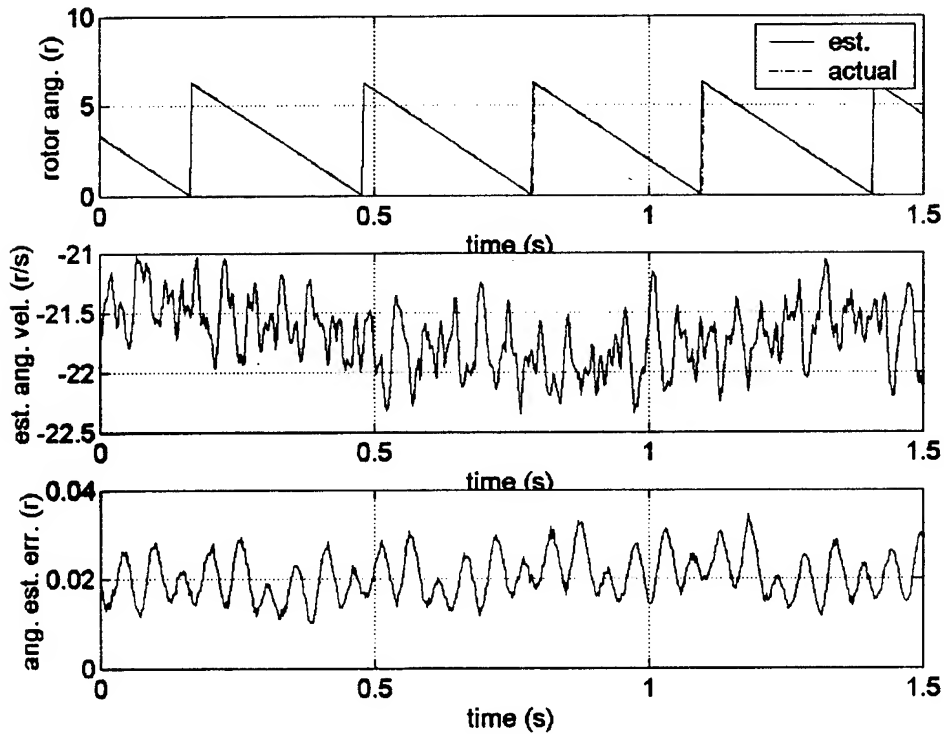


Figure 32. Estimation accuracy at 50 RPM, 15 ft-lb – low speed winding configuration.

For the sensorless drive system under consideration, the low-speed threshold was experimentally determined by viewing the estimated angular velocity at several low speeds. The speed at which the polarity reversals become quite infrequent represents a reasonable selection for the low-speed threshold. It has been the experience of the author that this low-speed threshold is typically 2% to 4% of the rated motor speed.

4.2.1.2 Steady State Rotor Position Estimation Robustness

In this section, the robustness of the developed sensorless PMSM drive is examined with respect to parameter uncertainty and external disturbances. In practical applications, machine parameters vary due to temperature effects. Therefore, an effective rotor position estimator must be robust to any uncertainty in the machine model.

The effect of load torque disturbances is shown in Figure 33 and Figure 34 for the low speed and high speed winding configuration, respectively. Recall that the model given in (6) and (7) does not contain mechanical variables such as torque, friction, and inertia in the state equations. Thus variations in the load torque are not expected to significantly affect the accuracy of the rotor position estimator. However, it should be noted that an increase in load torque requires a corresponding rise in the stator current. From the angle estimation error analysis of Chapter 2, it can be seen that a torque increase can cause a change in angle estimation accuracy if there is uncertainty in the motor inductance or resistance parameters, or if there exists errors in the current measurement. The predicted and experimentally certified immunity of rotor position estimation accuracy to load torque is verified in both Figure 33 and Figure 34. This represents a tremendous advantage over many other sensorless drive strategies that require estimation or direct measurement of the load torque.

The effect of stator inductance uncertainty on position estimation accuracy has been examined in Chapter 2. In the experiment depicted in Figure 35, the stator inductance used by the observer PMSM model is intentionally detuned by 50% from its actual value. Comparison of Figure 33 and Figure 35 show how the performance of the rotor position estimation accuracy is adversely affected by the changing load torque in the case of stator inductance uncertainty. Clearly, the inaccurate inductance used by the model results in degraded performance with increasing load (current) as predicted in Chapter 2.

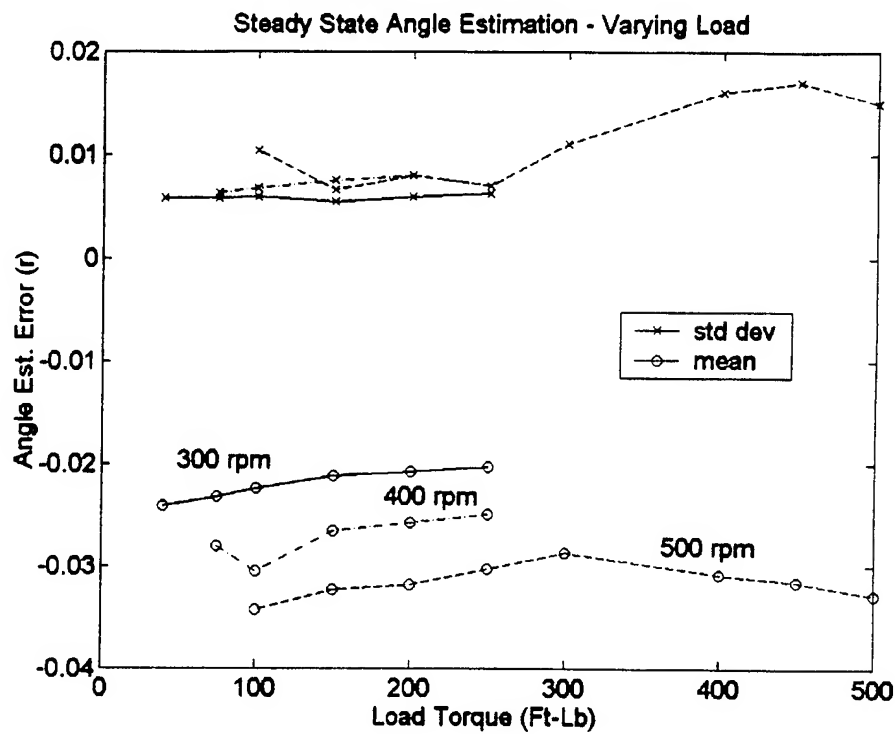


Figure 33. Estimation accuracy versus load torque at constant speed – low speed winding configuration.

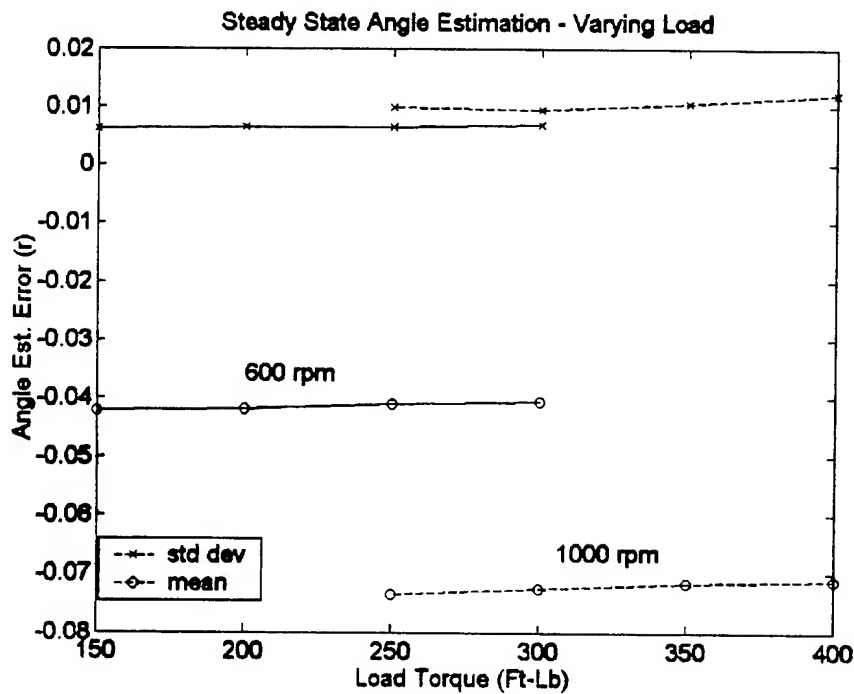


Figure 34. Estimation accuracy versus load torque at constant speed – high speed winding configuration.

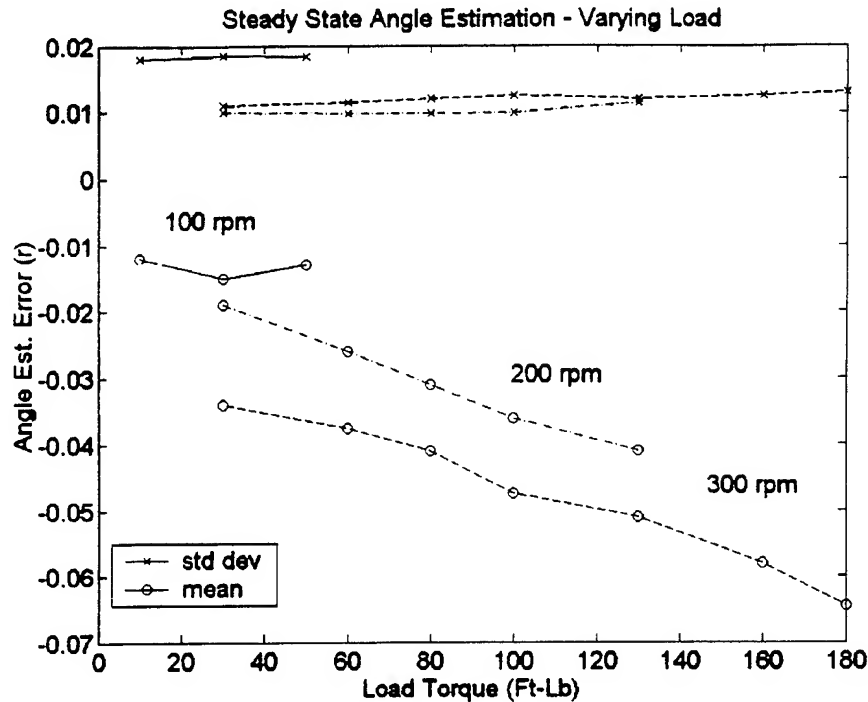


Figure 35. Estimation accuracy versus load at Constant Speed - low speed windings with stator inductance detuned by 50%.

In the PMSM, the machine parameters λ_m and R may vary inversely and proportionally with the temperature, respectively. The permanent magnet flux linkage parameter λ_m is not used in the machine model so that it is not expected to directly generate angle estimation errors. However, the parameter λ_m is used to estimate the angular velocity so that uncertainty in λ_m manifests itself as a velocity estimation error. Note, however, that even with the adaptive angular velocity estimation technique presented in Chapter 2, reasonable uncertainty in λ_m will not produce angular velocity errors in the steady state.

In Chapter 2, the effects of stator resistance uncertainty were examined. This study revealed that under normal operating conditions, stator resistance uncertainty has little effect on angle estimation accuracy. To verify this prediction, angle estimation error measurements were performed with the internal model parameters intentionally detuned by (an extreme) 300 percent. The results of this experiment are shown in Figure 36, where the top plots show performance with the actual resistance value. The bottom plots show system performance when the PMSM model uses a resistance value that is increased by 300% from its known value. In both cases, the motor was operating at 200 RPM with a load of 60 ft-lb. From a comparison of the results in Figure 36, the prediction set forth in the estimation error analysis of Chapter 2 is confirmed. It should be noted that the resistance parameter that is intentionally being detuned is also used to determine the values in the observer gain matrix G given in (23), and to determine the estimated angular velocity that is used to construct the time-varying system matrix (A_w).

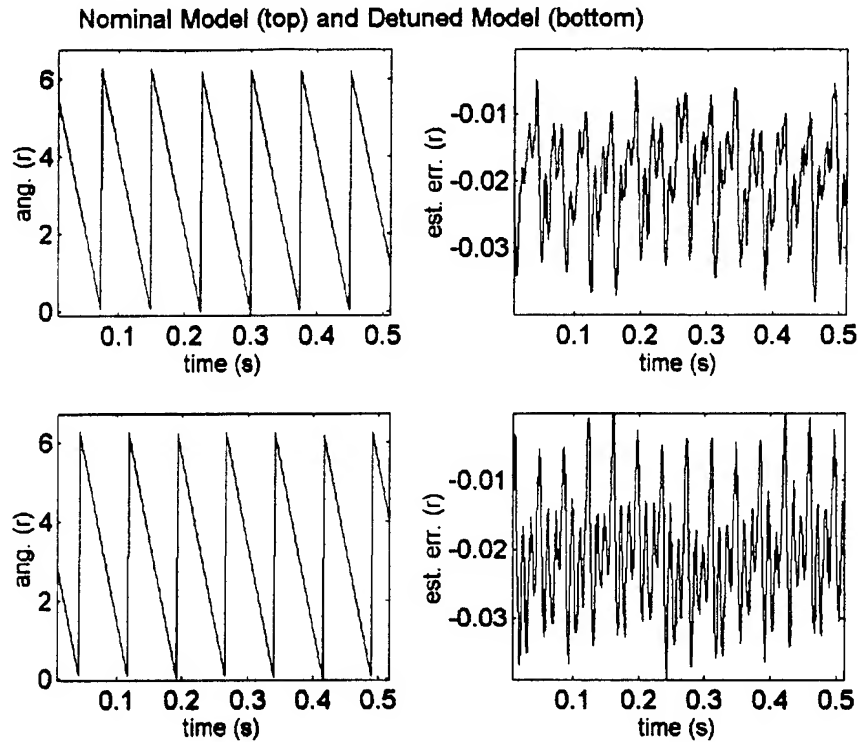


Figure 36. Estimation accuracy with actual (top), and detuned resistance values.

One concern in the implementation of a sensorless electric drive is related to the use of the line filter between the inverter and PMSM, as shown in Figure 24. When such a filter is utilized, it is important to sense the voltage and current at the filter output as shown in Figure 10, rather than at the inverter output. For this reason, the line filter presents difficulties in using the indirect voltage sensing method, as described in [18].

To examine the effects of the line filter on rotor position estimation, a set of experiments were carried out. The drive was operated at various RPM and load conditions both with and without the line filter in place, and the results were compared. An example of the test results is presented in Figure 37 and Figure 38, where the PMSM is operating at 200 RPM and 100 ft-lb load torque. Figure 37 shows the performance with the filter in place, while performance without the filter is shown in Figure 38. Comparison of these experimental results demonstrates little if any change in performance. This result was confirmed by the test results at other operating conditions across the range of the PMSM capabilities.

A complete plot of the measured quantities, estimated states, and estimated rotor angle is included in Figure 39 and Figure 40. Figure 39 is shown for the low-speed winding configuration operating at 500 RPM and 400 ft-lb. load torque. Figure 40 shows operation at 900 RPM and 400 ft-lb (70 HP). In each of these figures, note that the measured quantities (voltage and current) are shown in the stationary three-phase reference frame. All estimated values (flux linkages and currents) are shown in the two-phase stationary reference frame.

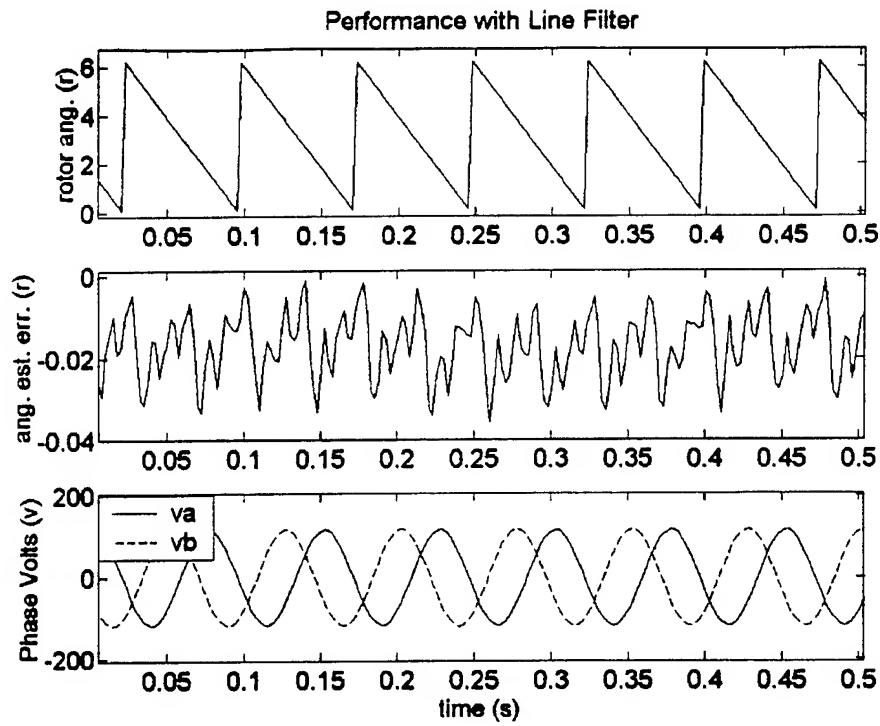


Figure 37. Angle estimation performance at 200 RPM, 100 ft-lb – with line filter.

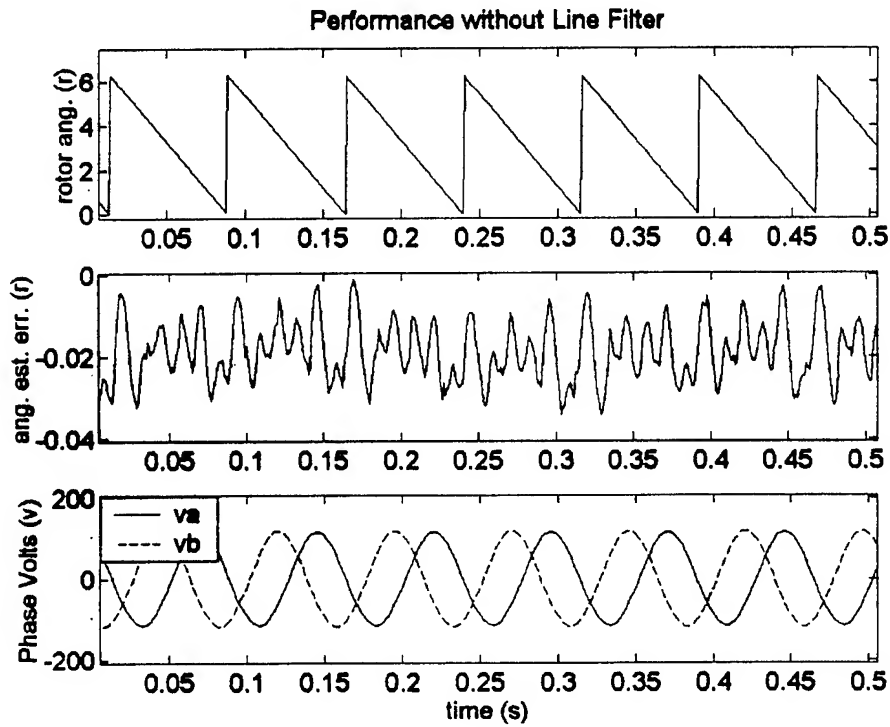


Figure 38. Angle estimation performance at 200 RPM, 100 ft-lb – without line filter.

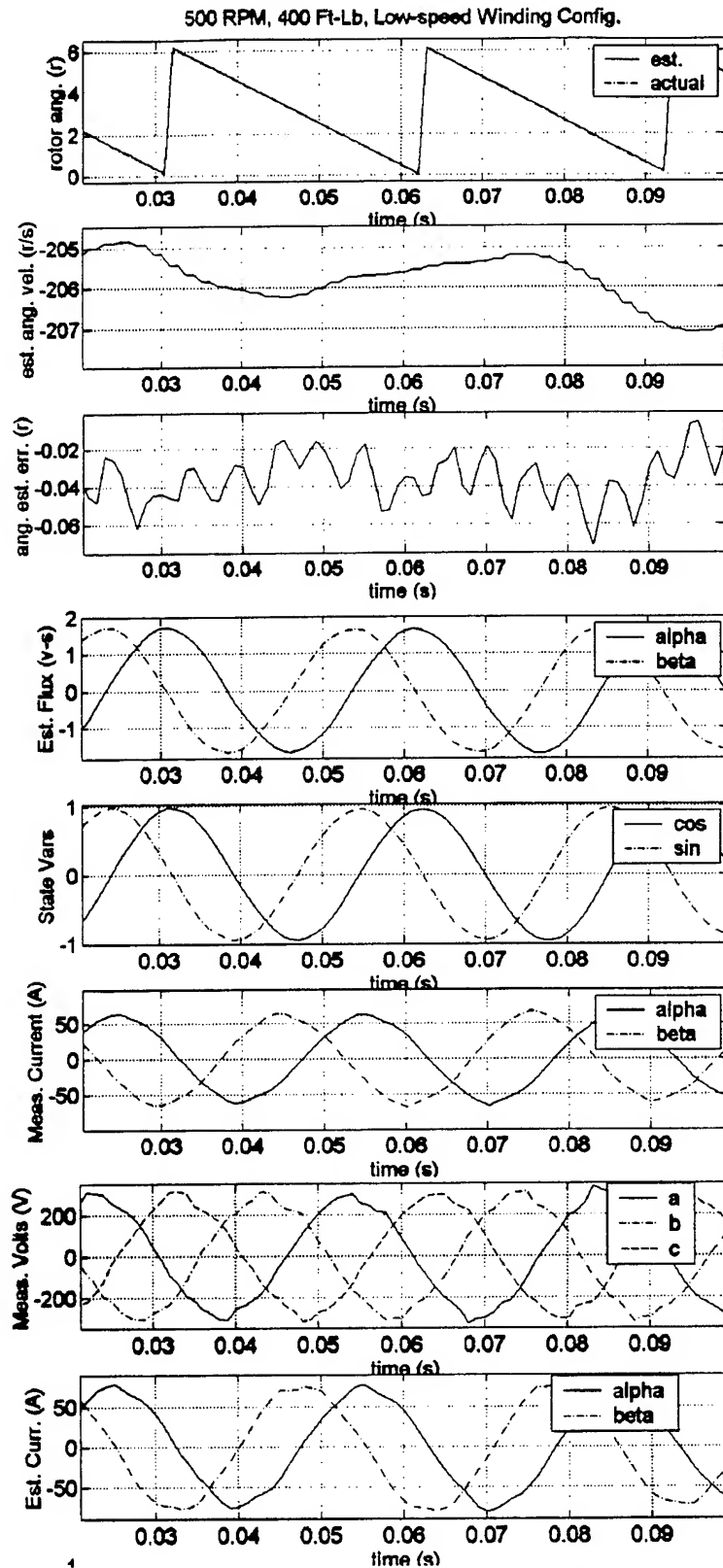


Figure 39. Measurements and state estimation for 500 rpm, 400 ft-lb load.

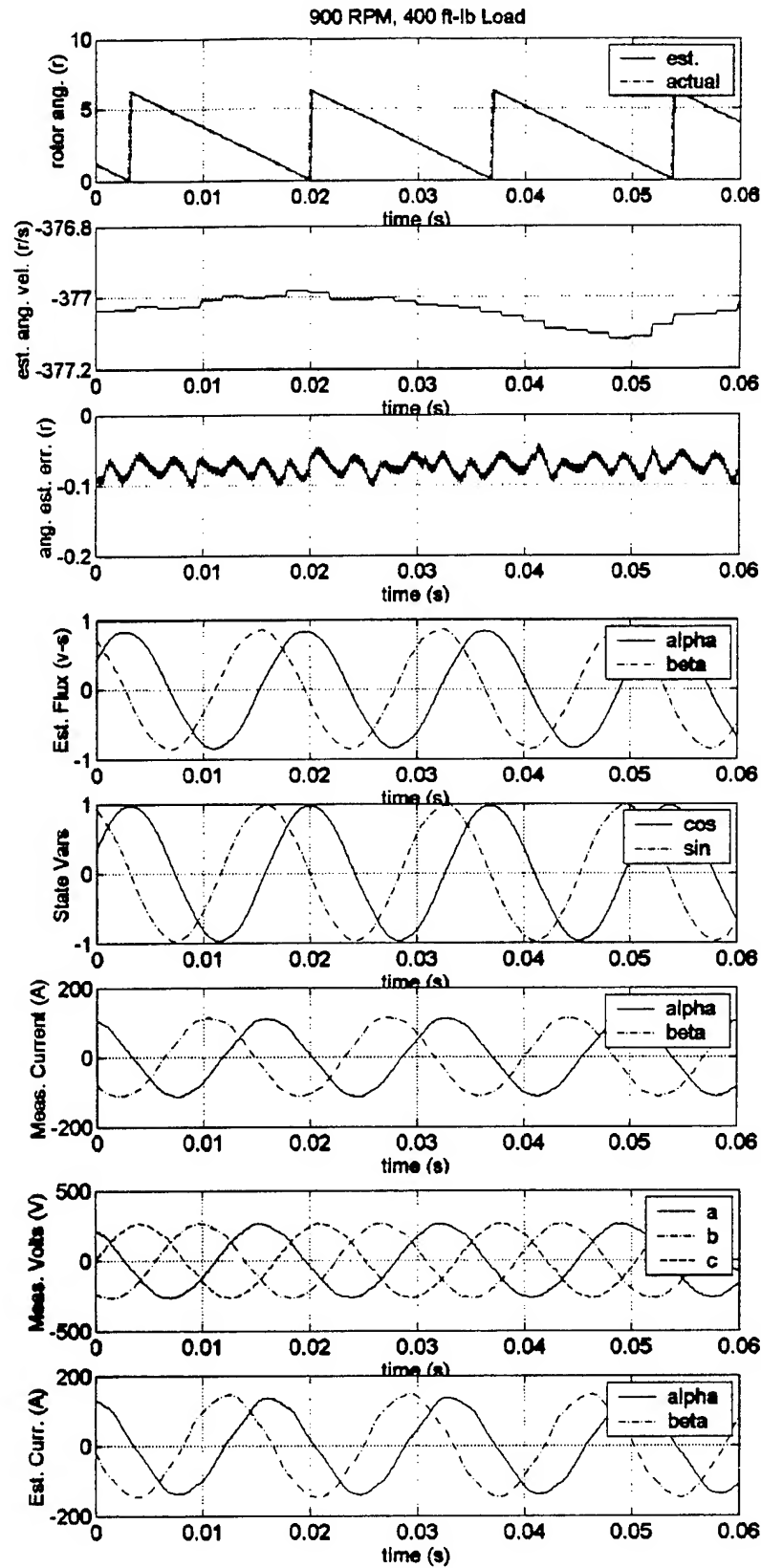


Figure 40. Measurements and state estimation for 900 rpm, 400 ft-lb load.

4.2.2 Transient Rotor Position Estimation Accuracy

During startup or speed reversal transients, the rotor velocity passes through the problematic zero speed range. Therefore, an examination of the transient performance of the sensorless drive is essential. In this section, the system performance is examined for several transient conditions, including startup and speed reversal.

4.2.2.1 Startup of Sensorless PMSM

It is well known that sensorless operation is problematic at standstill. At zero speed, general purpose principles for rotor position estimation usually fail due to the lack of an induced voltage in the stator windings. For the proposed rotor position estimator, the observer is ill-conditioned at zero speed because the last two rows of the system matrix A go to zero, rendering the system unobservable. Therefore, the position estimator is not usable at zero speed, and unless the initial rotor position is known, it is not possible to start the machine at full torque or to guarantee a dither-free startup.

For the sensorless drive demonstrator system, a specialized startup strategy is implemented that yields to the rotor position observer when a low-speed threshold is exceeded. More specifically, the demonstrator sensorless drive adopts the so-called *forced-alignment* technique [24]. The forced alignment technique applies a dc current to the stator before startup. The dc current acts to align the permanent magnet field with the magnetic field generated by the stator excitation, and forces the rotor to a known initial position. Since the initial position is known, torque can be applied to the PMSM at startup and the rotor position estimator operated in open loop configuration until the low-speed threshold is surpassed.

The initial torque applied to the PMSM at standstill after forced alignment must be sufficient to produce a rotational velocity that exceeds the low-speed threshold before the angle estimation error becomes excessive. In practice, this objective has been achieved to produce very reliable PMSM startup despite the lack of a position sensor. To demonstrate the startup procedure (after forced alignment) several illustrations are provided. In the startup depicted in Figure 41 where a startup velocity command of 200 RPM is issued, the low-speed threshold of 7.5 r/s is exceeded at 0.96 seconds. At that instant, the estimated rotor angle converges toward zero from an initial error of approximately 20 electrical degrees. Until the low-speed threshold is achieved, the system operates without feedback, with the estimated rotor velocity driving the harmonic oscillator that produces the estimated permanent magnet flux linkages in the two-phase stationary reference frame.

In Figure 42, each of the measured quantities (current and voltage) as well as the estimated state variables are shown for a startup sequence. For this experiment, a speed command of 300 RPM is issued, with the viscous load set to provide 180 ft-lb of torque at the commanded speed.

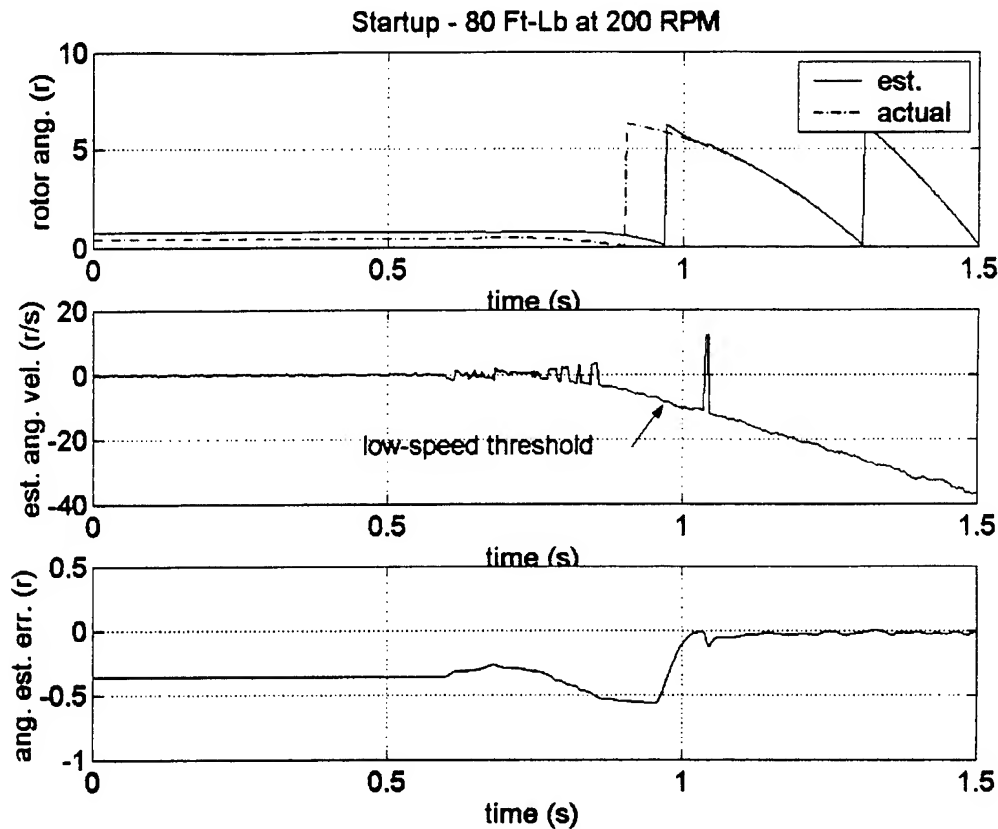


Figure 41. Startup from zero speed with load of 80 ft-lb at 200 RPM.

4.2.2.2 Speed Reversal

During a speed reversal, the rotor velocity passes through the problematic zero speed range. While the magnitude of the estimated rotor velocity is below the low-speed threshold, the rotor position observer operates without feedback. Such operation has been shown through experimentation to be acceptable for short time intervals, such as during a speed reversal. In Figure 43, the rotor position observer is examined during a speed reversal. In the figure, the estimated velocity magnitude drops below the threshold at 1.75 sec. And the observer operates without feedback until 1.9 seconds, where feedback is restored. From the estimated states in the figure (flux linkage and trigonometric functions of the rotor angle) it is seen that the open-loop model produces excellent results, or ride-through capability, for short term operation below the low-speed threshold.

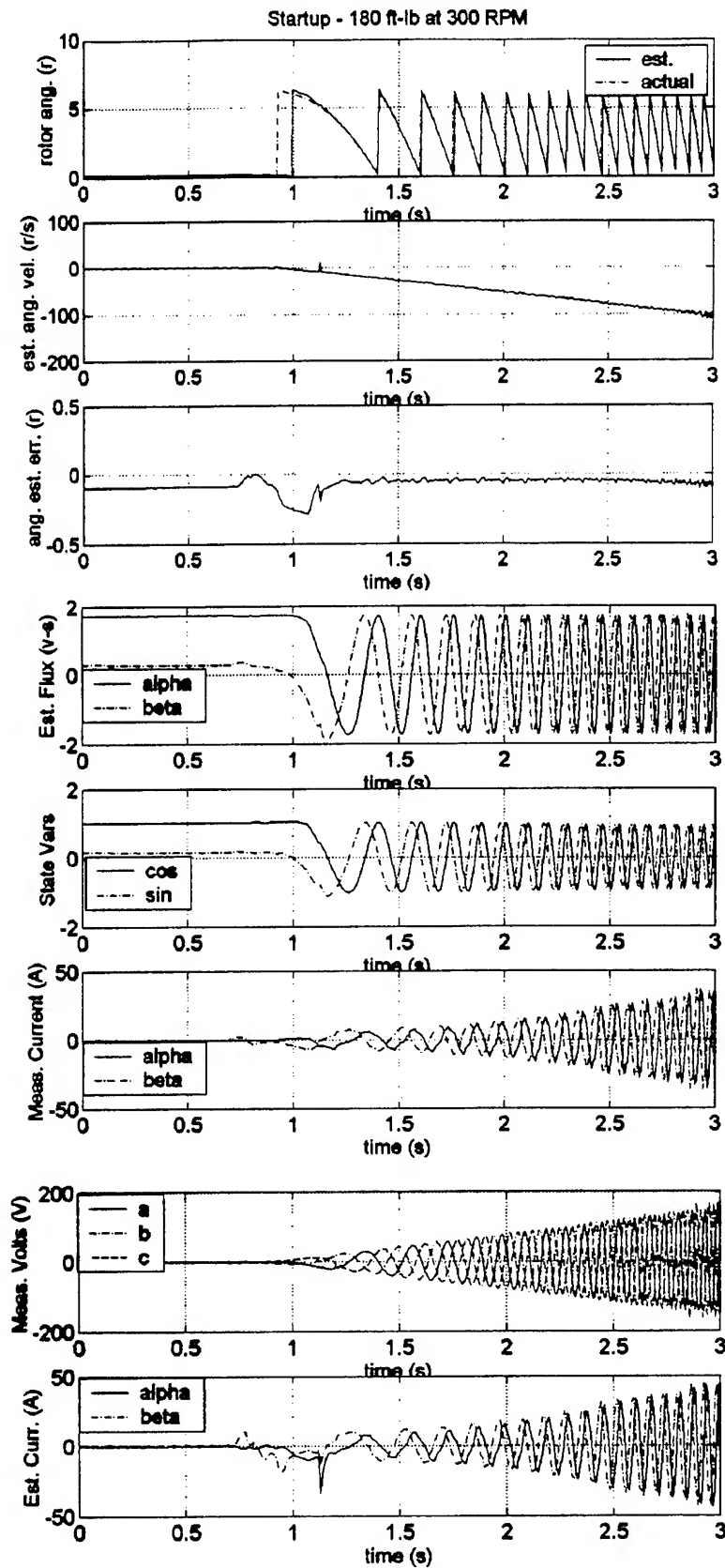


Figure 42. Startup from zero speed with load of 180 ft-lb at 300 RPM.

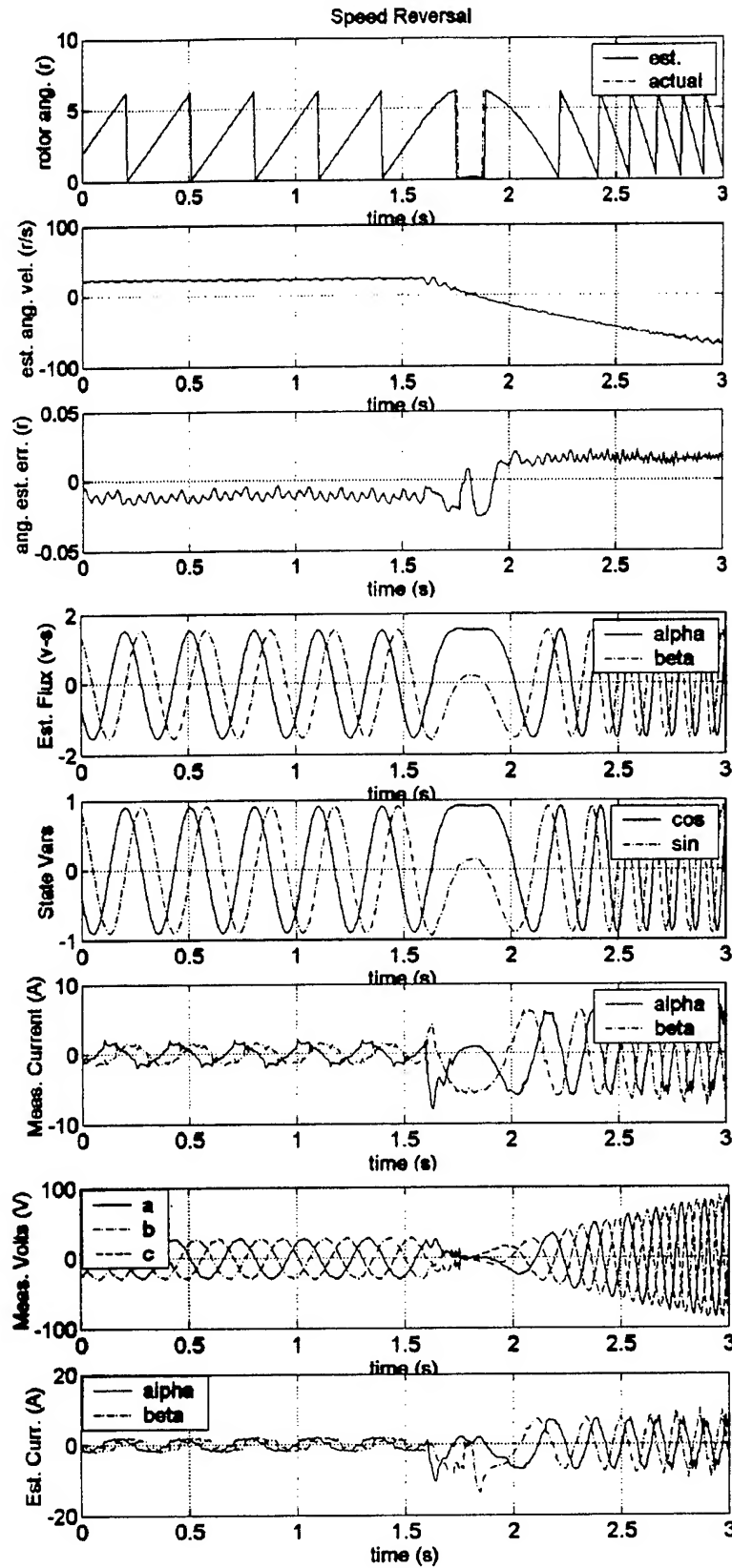


Figure 43. Speed reversal of PMSM – state variables and measured quantities.

4.3 Acoustic Performance

To quantify the effects of the sensorless drive on acoustic performance, a set of self-noise measurements are to be performed on the drive, and compared with sensed operation of the same motor. As indicated in the original proposal, these tests will be provided to ONR for at least the first two water tunnel tests that use the developed sensorless drive system. At the time of this writing, there have not been any water tunnel tests scheduled to utilize the PMSM and thus the data is not yet available. An addendum to this document will be generated at the time this acoustic measurement data becomes is obtained. As indicated in the proposal, the cost for these tests will be absorbed by ARL.

5 CONCLUSIONS

This work has presented the design and implementation of a sensorless electric drive for a high power permanent magnet synchronous motor (PMSM). The developed sensorless drive is implemented in a real-time motor drive system, and is shown through extensive experimentation to be robust to model uncertainty and disturbances, while providing very accurate rotor position estimation. The angle estimation accuracy demonstrated by the proposed technique exceeds the published accuracy data from other laboratory sensorless drive implementations. Furthermore, the proposed technique has been shown to be immune to mechanical parameters and disturbances, which are difficult to determine and are often unknown.

The primary remaining issue associated with the use of the sensorless drive in a propulsion system is the implementation of a high-performance velocity controller. Due to the high accuracy demonstrated by the rotor position estimator, current control performance approaches that of a fully sensed drive, with clear advantages of sensor-based control only evident around zero speed. The lack of a velocity sensor in the sensorless system, however, presents a serious challenge in achieving accurate velocity tracking. As discussed in the text, the adaptive velocity estimation technique provides accurate velocity feedback in the steady state, but low-pass filtering with a very slow time constant is required to remove ripple from the estimated angular velocity. If the ripple is not removed, the torque control loop suffers, and smooth torque is not generated. Excessive filtering of the estimated velocity, however, degrades the transient performance of the system.

Issues related to sensorless PMSM startup have been addressed in this document through the adoption of a forced alignment technique. This technique has been shown through experimentation to provide reliable PMSM startup.

In summary, the results of this study suggest that the sensorless electric drive is a viable alternative for electric drive applications such as rim-driven propulsion topologies. The sensorless drive implementation and experimental results discussed in this study will serve as valuable information for any future sensorless drive design endeavors.

6 ACKNOWLEDGEMENTS

The following personnel offered valuable assistance and feedback during the course of this project:

Tom Calvert, NSWC Carderock
Lynn Petersen, NSWC Carderock
Mark Turner, Applied Research Laboratory
Brian Kline, Applied Research Laboratory
Jim Mickey, Applied Research Laboratory
Dr. K.Y. Lee, Pennsylvania State University Dept. of Electrical Eng.
Daniel Thivierge, NUWC Newport

The author is also grateful for the support from the Office of Naval Research through Grant Number N00014-00-G-0058/0007

- [1] T.D. Batzel, "Sensorless Electric Drive for Permanent Magnet Synchronous Motors", Final Report – Applied Research Laboratory Technical Report No. TR-99-006, Oct. 1999. Funded by ONR under Grant N00014-98-1-07187.
- [2] S. Chung, H. Kim, C. Kim, M. Youn, "A new instantaneous torque control of permanent magnet synchronous motor for high performance direct drive applications", Applied Power Electronics Conference and Exposition, 1997, v. 2, pp. 721-727.
- [3] L. Zhong, M. Rahman, W. Hu, K.Lim, "Analysis of direct torque control in permanent magnet synchronous motor drives", IEEE Transactions on Power Electronics, v. 12, no. 3, May 1997, pp. 528-536.
- [4] S. Morimoto, Y. Tong, Y. Takeda, T. Hirasaka, "Loss minimization of permanent magnet synchronous motor drives", IEEE Transactions on Industrial Electronics, v. 41, Oct. 1994, pp. 511-517.
- [5] S. Bogosyan, M. Gokasan, "Adaptive torque ripple minimization of permanent magnet synchronous motors for direct drive applications", IEEE Industry Applications Conference, v. 1, 1995, pp. 231-237.
- [6] T. Batzel, K.Y. Lee, "Commutation torque ripple minimization for permanent magnet synchronous motors with Hall effect position feedback", IEEE Transactions on Energy Conversion, v. 13, Sept. 1998, pp. 257-262.
- [7] S. Clenet, Y. Lefevre, N. Sadowski, S. Astier, "Compensation of permanent magnet motors torque ripple by means of current supply waveshapes control determined by a finite element method", IEEE Transactions on Magnetics, v. 29, March 1993, pp. 2019-2023.
- [8] P.L. Chapman, S.D. Sudhoff, C.A. Whitcomb, "Optimal current control strategies for surface-mounted permanent magnet synchronous machine drives" IEEE Transactions on Energy Conversion, vol. 14, No. 4, December 1999, pp. 1043-1050.
- [9] C.P. Cho, L. Smith, W. Fennell, J. Raposa, W. Krol, J. Uhlman "A novel integrated electric motor/propulsor for underwater propulsion", Naval Symposium on Electric Machines Proceedings, October 1998, pp. 3-8.
- [10] T. Batzel, K.Y. Lee, "Slotless permanent magnet synchronous motor operation without a high resolution rotor angle sensor", IEEE Transactions on Energy Conversion, vol. 15, no. 4, Dec. 2000, pp. 361-365.
- [11] D. Luenberger, D. "An introduction to observers," IEEE Transactions on Automatic Control, vol. AC-16, no. 6, pp. 596-602.
- [12] W.L. Brogan, *Modern Control Theory*, Prentice-Hall, Englewood Cliffs, NJ.
- [13] C. Phillips and R. Harbor, *Feedback Control Systems*, Prentice Hall, Englewood Cliffs, NJ.
- [14] R. Krishnan and R. Ghosh, "Starting algorithm and performance of a PM DC brushless motor drive system with no position sensor," Power Electronic Specialists Conference (PESC), pp. 815-821.
- [15] R. Wu and G. Slemon, "A permanent magnet motor drive without a shaft sensor," IEEE Transactions on Industry Applications, vol. 27, no. 5, pp. 1005-1011.
- [16] T.D. Batzel and K.Y. Lee, "Commutation torque ripple minimization for permanent magnet synchronous motors with Hall effect position feedback," IEEE Transactions on Energy Conversion, v. 13, no. 3, pp. 257-262.
- [17] T.D. Batzel and D.P. Thivierge, "Electric drive for 21" UUV," 3rd Naval Symposium on Electric Machines, Philadelphia, PA.
- [18] T.D. Batzel, "Electric propulsion using the permanent magnet synchronous motor without rotor position transducers," Pennsylvania State University Ph.D. Defense, December, 2000.
- [19] Z. Lin, D. Howe, P. Mellor, and M. Jenkins, "Coupled thermal and electromagnetic analysis of a permanent magnet brushless dc servo motor," Proceedings of the 6th International Conference on Electric Machines and Drives, 1993, pp. 631-635.
- [20] W. Leonhard, *Control of Electrical Drives*, Springer-Verlag, New York, NY, 1985.
- [21] J. Holtz, "Pulsewidth modulation – a survey," IEEE Transactions on Industrial Electronics, vol. 39, no. 5, Dec. 1992, pp. 410-420.
- [22] J. Moynihan, M. Egan, and J. Murphy, "The application of state observers in current regulated PM synchronous drives," Proceedings of the 20th International Conference on Industrial Electronics, Control, and Instrumentation IECON), 1994, vol. 1, pp. 20-25.

-
- [23] J. Choi, H. Kim, and S. Sul, "*Design of fast response current controller using d-q axis cross-coupling*," Proceedings of the 22nd International Conference on Industrial Electronics, Control, and Instrumentation (IECON), 1996, vol. 2, pp. 1187-1192.
- [24] N. Matsui and M. Shigyo, "*Brushless DC motor control without position and speed sensors*," IEEE Transactions on Industry Applications, vol. 28, no. 1, 1992, pp. 120-127.